pEDFM (Projection-based Embedded Discrete Fracture Model) on Corner Point Grid for mass transport in fractured heterogeneous porous media

Janio Piguave Tomalá

Student ID: 4862990

Faculty of Civil Engineering and Geosciences, TU Delft
18 November 2020

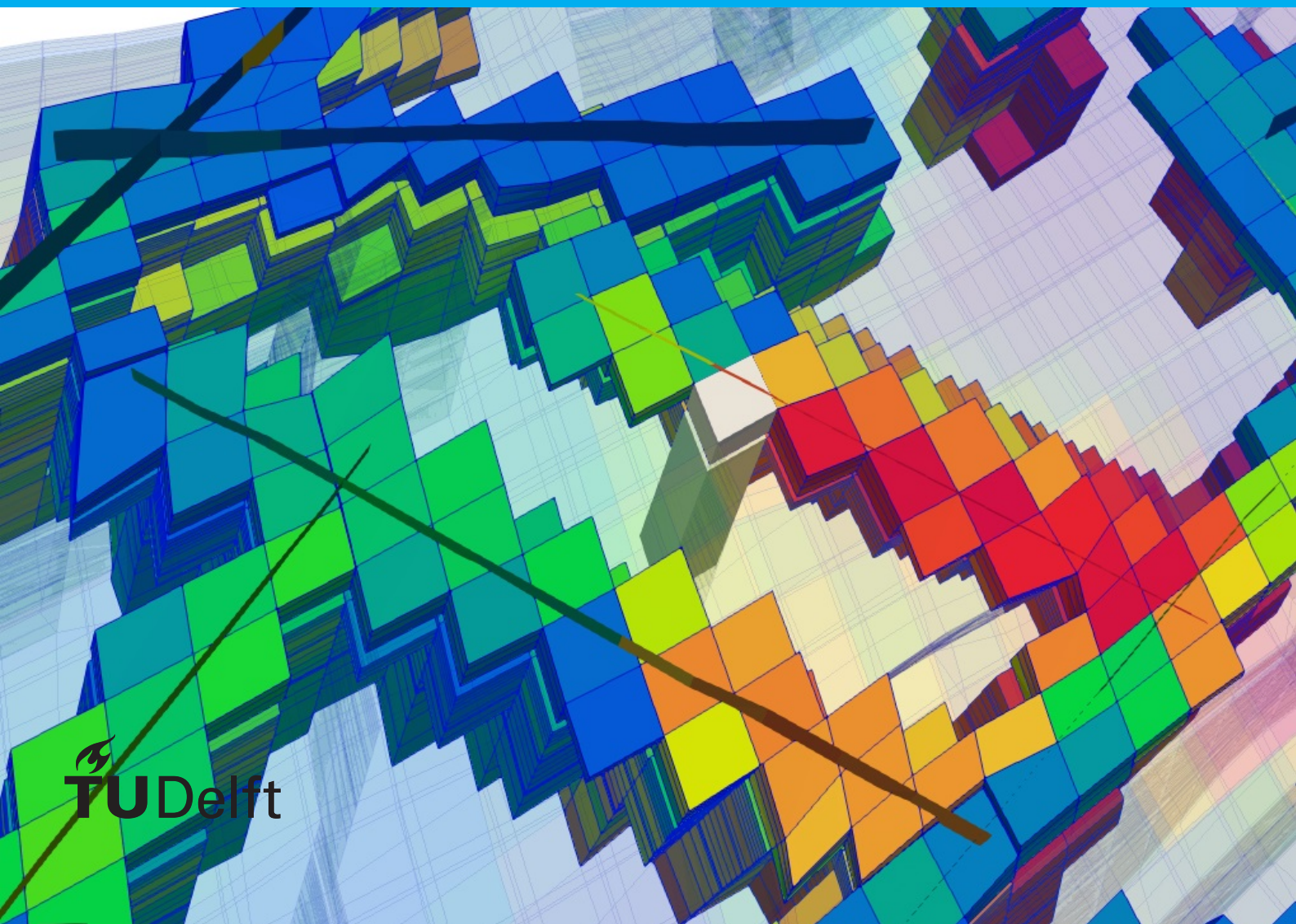

pEDFM (Projection-based Embedded Discrete Fracture Model) on Corner Point Grid for mass transport in fractured heterogeneous porous media

by

Janio Piguave Tomalá

to obtain the degree of Master of Science
at the Delft University of Technology,
to be defended publicly on Wednesday November 18, 2020 at 15:30 PM.

Student number:	4862990	
Project duration:	November 1, 2019 – October 31, 2020	
Advisor:	Associate Prof. Hadi Hajibeygi	CITG, TU Delft
co-supervisor:	Ir. Mousa HosseiniMehr	CITG, TU Delft
Thesis committee:	Associate Prof. Deyan Draganov	CITG, TU Delft
	Dr. Yuhang Wang	EWI, TU Delft

This thesis is confidential and cannot be made public until November 18, 2020.

TU Delft

Preface

Firstly, I express thanks to my supervisor Prof. Hadi Hajibeygi to be part of the DARSim team and provide guidance on my thesis project. I admire your passion for science; you are a person who inspires and continuously has motivated me to establish challenges through the development of my research and overcome them. I am grateful for the knowledge and wisdom shared during this period, as I will keep it after this academic experience.

I also express my gratefulness to my daily supervisor, Mousa Hosseinimehr, for your time and constant help. Your knowledge shared with me is part of this work, and undoubtedly your guidelines provided allow me to finish this project.

Thanks to my family, especially to my beloved mother, for their unconditional support. Thanks for always believing in me, backing my life decisions, and this recent venture to the Netherlands.

I want to thank TNO (Netherlands Organisation for Applied Scientific Research) to make the Brugge Model data set available for use in the present work.

Finally, thanks to the Ecuadorian Government and the Secretaría Nacional de Educación Superior, Ciencia y Tecnología (SENESCYT) for the scholarship awarded in 2017 that allowed me to travel to the Netherlands and obtain my graduate degree at Delft University of Technology.

Janio Piguave Tomalá
Delft, November 2020

Abstract

Regular Cartesian grid models provide satisfactory numeric results when a numerical scheme for reservoir flow simulation is applied. However, they cannot recreate complex geological features existing in realistic reservoir models such as faults and irregular reservoir boundaries. Corner point grids can represent these geological characteristics and can be adapted and represent any reservoir. In the subsurface reservoirs is usually typical to find fractures networks, and it is necessary to simulate the effect of them in reservoir models based on corner point grids. Although several works validate the precision of Embedded Discrete Fracture Model (EDFM) for representing fractures in cartesian grids, very few studies have been presented to examine the accuracy of fracture modeling in geologically complex reservoir models. In this work, the novel discrete fracture model, the Projection-based Embedded Discrete Fracture Model (pEDFM), is implemented to represent fractures in reservoir models based on corner point grids. pEDFM provides additional features to the EDFM and is applied to explicitly and consistently define fractures. It implements independent grid sets for the fractures (described as lower-dimensional domains) and the rock matrix irrespective of the grid domains' complex geometrical shapes. The suitability of the original pEDFM method has been expanded to a fully generic 3D geometry, and it lets on including fractures with any orientation on the corner-point grid cells, an important development for the method's viability in field-scale applications. Further to the geometrical flexibility of EDFM, matrix-matrix and fracture-matrix connectivities are re-adapted to account for the projection of fracture plates on the interfaces. This allows for consistent modeling of fractures with generic conductivity values, from high conductive networks to impermeable flow barriers. A fully implicit scheme is used to get a discrete system with two main unknowns (i.e., pressure and phase saturation) on both matrix and fracture networks. Several 3D test cases of reservoirs models with complex corner point grids and fracture networks arbitrary designed in them are presented to demonstrate the devised method's accuracy and applicability. The results show that the pEDFM implementation for two-phase flow is highly successful for modeling fractures with a broad range of conductivity on field-scale reservoir models.

Contents

1 Introduction

Optimization of hydrocarbon recovery, the management and sustainable use of the earth's water reserves, the sustainable use of geothermal energy, and recently the carbon sequestration in subsurface rock formations are four examples of current engineering challenges that subsurface flow theory can help to tackle them. The development of a reliable computer modeling of subsurface flow is necessary to overcome the difficulties related to the mentioned challenges. Reservoir simulation is the mean that helps us evaluate and predict how fluids flow through the subsurface. A simulation model comprises three components: a mathematical flow model that defines how fluids flow in a porous medium, a geological model that depicts the reservoir rock formation, and a model for the production process.

As a matter of simpleness, when a new mathematical model is formulated for solving a challenge in reservoir simulation, it is usually tested in a simplified reservoir geometry model. Cartesian grids are the predicted choice to apply them as they provide the perfect framework for testing new ideas. However, the Cartesian grids do not allow us to create a model that properly represents the geological reservoir's geometry. Realistic reservoir models are more conveniently described by flexible grids ([51] [34]). The denominated corner point grids ([53] [45] [10]), another structured grid, are a standard grid model in the industry. These grids can be distorted to generate geological features like faults and erosion surfaces present in the subsurface reservoir. Once it has been developed grid formats for modeling representative reservoir models, it is essential to remember that many reservoirs can contain natural fracture networks with an extensive range of conductivities ([6]). Fractures generally have tiny apertures (size of millimeters), and their volume is relatively small, but they need to be represented since they have a considerable impact on flow patterns. The EDFM was introduced to represent fractures without the necessity that the simulation grid must conform to the fracture geometry. The idea of the EDFM is to create different domains for matrix and fractures. It generates the matrix grid independent of the fractures' location in the matrix domain and defines flux interactions to link the separate domains.

The representation of fractures on structured Cartesian grids has been significantly referred to in the literature ([29] [30] [32] [18] [40] [47]). However, the EDFM scheme study in corner point grids models has not yet been wholly addressed so far ([33]). The following improvements of the original EDFM formulation have provided a method for reliable treatment of fractures with any conductivity ranges. This method is known as the projection-based embedded discrete fracture model (pEDFM) ([50] [21]), initially developed for single and multiphase flows. Additional research on pEDFM has been made to study the application of the method ([27] [20]).

Expanding the application of pEDFM from cartesian grids to corner point grids is a step to take the ideas of the method to be applicable in the industry. To provide usefulness for commercial applications, it is necessary to show that pEDFM can model explicit fractures in reservoir geometries representing the subsurface structures' inherent complexity. The mentioned facts allow us to study the performance of pEDFM formulation and in corner point grid domains.

In this thesis, a pEDFM implementation on a corner-point grid domain is presented. The simulation of isothermal two-phase mass flow in fractured porous media is performed in an open-source reservoir simulator. The discrete non-linear fully implicit (FIM) system is obtained for two main unknowns: pressure and saturation, on both matrix and fracture network, and solved using the Newton-Raphson iterative method. pEDFM is used to represent fractures explicitly and consistently and to provide in-

dependent gridding of matrix and fractures regardless of complex geometrical shapes of domains. Further to the geometrical flexibility of EDFM, the matrix-matrix and fracture-matrix connectivities are modified to include the projection of fracture planes on the interfaces. It results in a scheme that allows consistent modeling of fractures with generic ranges of conductivity.

Finally, the pEDFM implementation is tested in several studies in 3D reservoirs models. A verification study is performed to validate the pEDFM model for fracture modeling in a cartesian and corner point model. Then, several benchmark reservoirs models are used, with their petrophysical properties, and fracture networks arbitrary designed for each of the models to demonstrate the devised method's accuracy and applicability.

1.1. Reservoir Grids

A subsurface reservoir is sketched for two types of surfaces, lateral surfaces that establish geological horizons that delimit the different stratum and vertical or inclined surfaces representing faults.

The geological reservoir is a continuous model, and some parameters change with the fluid flow over time. It is essential to define an approach to track these parameters changes, but it is impossible to obtain that with the continuous model. A reservoir simulator requires as input a discretized version of that continuous reservoir model. Hence, it is necessary to split the continuous reservoir into a finite number of discrete components that characterize time development in a discrete approach. The reservoir's discretization is defined as the reservoir's subdivision into finite volume elements or cells, and this set of elements is known as the reservoir grid. In brief, reservoir simulation uses a numerical model of the subsurface reservoir and the multiphase fluid system to evaluate and forecast how fluids flow through the reservoir rock throughout time.

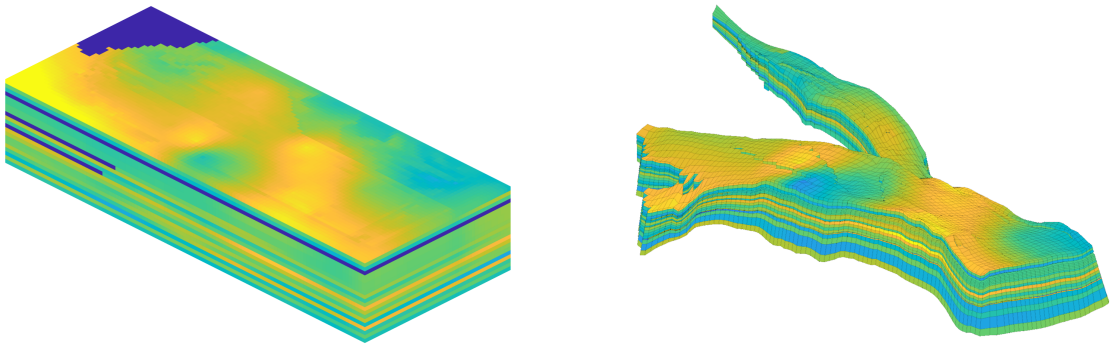

Figure 1.1: A Cartesian grid model can be interpreted as representing the reservoir model at geological "time zero," when the sediments have formed a stack of horizontal grid layers due to deposition (left plot). From geological time zero to the present, geological activity has created faults and distorted the layers, creating a structural model (right plot).

Furthermore, to expect representative simulation results, it is required that the grid should be a reliable representation of the reservoir structure. In the first place, the geological features of the reservoir, such as stratified layers, pinch outs, unconformities, faults, channels, and irregular boundaries, have a considerable influence on the flow patterns and simulations results. Also, the high heterogeneity of the reservoir's rock properties represents a challenge for gridding definition since the grid blocks should have constant values for the petrophysical parameters. On top of this, the grid's purpose is to represent a tool for numerically solving the reservoir flow equations. The mathematical model implemented for flow simulations should be suitable with the grid type chosen to reach reliable simulation results.

The ideal grid cells for reservoir simulation are the cartesian ones. A regular cartesian grid consists of congruent rectangles in a 2D domain and rectilinear parallelepipeds in a 3D domain, and it is implied that all cell faces encounter right angles. However, these rectangular grids do not permit a suitable approximation of complex reservoir geometry since they cannot adapt to the geological features before mentioned.

Unstructured grids [28] [26] (Delaunay triangulations and Voronoi grids) represent another grid option for model the geological features in reservoir models. An unstructured grid consists of polyhedral cells with varying faces that are settled in an irregular pattern. Unstructured grids can adapt to any geometry, and for a particular domain, the total number of grid cells keeps at a manageable level, en-

abling running a simulation. Despite the benefits of using unstructured grids, it is possible to consider other structured grids, which are the denominated corner point grids. The main advantage of them is allowing easy implementation in standard reservoir simulations as they keep some aspects of cartesian grids, which has made the corner point grid the industry's standard grid format.

1.2. Fracture Modeling

Naturally fractured reservoirs (NFRs) are the reservoirs that contain natural fracture networks. These systems are difficult to characterize and predict, but it is not possible to deny their influence on reservoir performance. Comprehensive knowledge of multiphase fluid flow behavior in such systems is vital in many applications such as hydrocarbon recovery, geothermal energy exploitation, and aquifer management.

It is necessary to find a precise and efficient representation of these structural features with the suitable numerical solution techniques. There are two standard numerical methods developed to perform flow simulations for NFRs:

- Continuous representations: Dual-porosity / dual-permeability (DP/DK) approach.
- Discrete representations: Discrete fracture modeling (DFM) approach.

Continuum types of models assumes that the fracture network must be mainly connected among their elements. The properties and geometry of the fracture system remain continuous. DP/DK models are prone to homogenize the fractures that play a role in the flow through disregard the connectivity with the grid cells. Also they provide inaccurate solutions in high heterogeneity fracture systems. The transfer term required to join the parallel continuous system (fracture and matrix) can be difficult to define when gravity and capillarity are included. The mentioned facts of the continuum modes limit their pertinence to represent realistic fracture networks.

Another alternative for fracture modeling can provide better results: the discrete fracture model (DFM). The DFM approach separates fractures in a lower-dimensional system and combines it with the matrix through a transfer function as discrete representations. DFM is employed to simulate realistic fracture geometries and can precisely represent the effects on fractures' fluid flow.

1.3. Discrete Fracture Models (DFM)

DFM ([28] [46] [51]) has been applied through different approaches: the Conforming DFM (CDFM) and the Embedded DFM (EDFM). The difference between the two models lies in the way how the grid for matrix rock and fractures is generated.

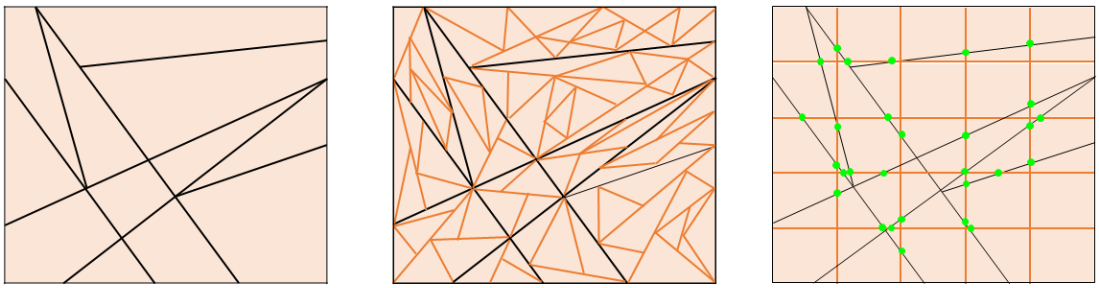

Figure 1.2: Grid construction of two different DFM approaches: CDFM (unstructured matrix grid) (center) and EDFM (structured matrix grid) (right).

In CDFM, unstructured grids are used to conform to the geometry and position of the fractures. Mass transfer between fractures and matrix is represented by modifying the transmissibility of fracture - matrix interfaces. However, a complex fracture network will generate a high number of grid cells to represent it, which will demand a high computational cost to solve the linear systems. The small size of some fractures grids may affect the results of the numerical solutions. It is also inefficient since the matrix grid must be redefined at each time step in dynamic environment simulations (fracture generation and propagation).

On the other hand, EDFM discretizes the matrix and the fractures separately, and a flux transfer term is used to couple them. One main advantage of EDFM is the possibility of modeling the matrix even with simple grids in the presence of complex fracture networks due to the independent grids for fractures and matrix. The main restriction of EDFM is the inability to model fractures with low conductivity contrasted to the matrix. The novel projection-based embedded discrete fracture model (pEDFM) provides a solution to this problem, which allows modeling fractures with a wide range of permeabilities [50].

1.4. Research Goals

This MSc thesis report's primary goals are implementing the pEDFM approach for fracture modeling in corner point grids models. Therefore, the research goals of this thesis can be summarized as the following:

- Development of a pEDFM implementation on corner point grids in an open-source simulator.
- Test the pEDFM implementation in realistic reservoir models available on public data sets.

The thesis is structured as follows. In chapter 2, an introduction to corner point grids is briefly described. In chapter 3, EDFM and the implementation of pEDFM for corner point grid models is explained. Then, in chapter 4, a brief description of the public data sets used in this work is presented. In chapter 5, the test results and discussions for the results of the implementation of pEDFM in corner point grid models are covered. Finally, conclusions are presented in chapter 6.

2

Corner Point Grids

After it has been revised an overview of the different grids used in reservoir simulation, the corner point grids ([53] [45] [10]) are introduced in this chapter.

2.1. Structured grids

Structured grids can be described with two main characteristics:

- Grid cells are six-sided with eight nodes.
- Grid cells are logically organized in a common framework, such that its $i-j-k-$ index exclusively determines each cell's location in the grid.

2.2. Description

A corner point grid system can be considered as a standard rectangular grid block system distorted, which is achieved by allowing each grid block to be defined by its eight corner points. The corner points are established in a suitable ordering as they describe well-defined volumes. The cell geometry is complemented with bilinear planes as surfaces, and the placement of grid cells should avoid overlaps between them [10] [45].

The grid is defined with non-horizontal lines (coordinate lines or pillars) delineated by their endpoints over a cartesian 2D mesh in the lateral direction. A constant number of corner-point nodes are set on every non-horizontal line, and each cell in the grid is established between four neighboring pillars and two adjacent points on each non-horizontal line.

A fictitious domain approach is used to insert the complex reservoir model into a logically Cartesian domain. The inactive cells that are not part of the active physical model are also present in the topological $i-j-k-$indexing. A Boolean indicator value is defined in each cell to indicate if the cell is part of the active domain or not.

As corner point grid is a structured grid, they are topologically ordered in a logically cartesian manner, meaning that each cell has been assigned and i $i-j-k-$index, with $1 \leq i \leq n_i$, $1 \leq j \leq n_j$, $1 \leq k \leq n_k$, and the grid consists of $n_i \times n_j \times n_k$ grid cells. The k-index is understood to be related to the vertical direction (depth), and cells that share a grid and have the same $i-$ and j-indices, but different $k-$indices, are supposed to create a vertical stack.

2.3. Degeneracy of grid cells

The advantage of the corner point grid is handling the eight-cell corners' position to adapt and recreate geological features in the reservoir model. For establishing more accurately vertical and inclined faulting, it is advantageous to define the grid cell's position by its corner point locations and displace them along the coordinate lines aligned with faults surfaces. Similarly, for modeling erosion surfaces and pinch-outs of geological layers, the corner point format allows corner points to collapse along coordinate lines. The corner points can collapse along all four coordinate lines so that the cell completely

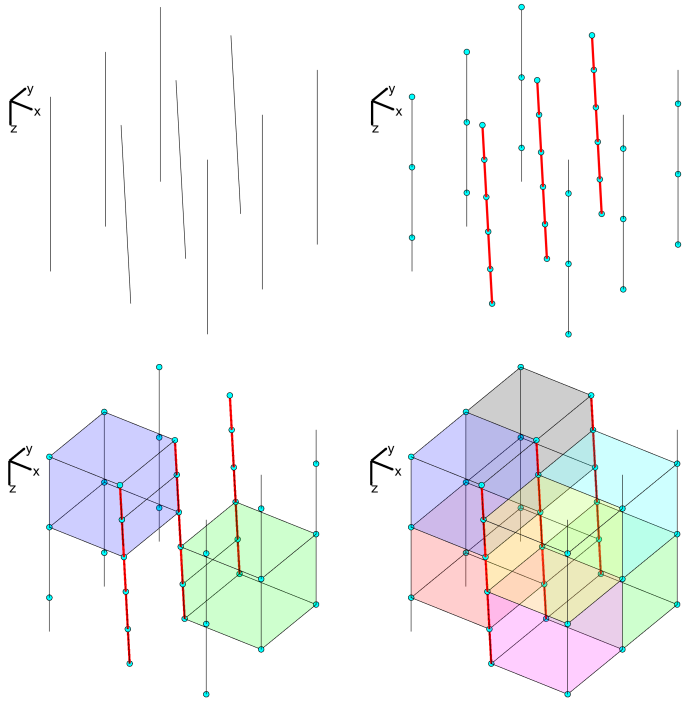

Figure 2.1: Construction of a corner-point grid. Starting from the coordinate lines that defining pillars (upper left), corner-points and identify lines containing nonmatching corner marked in red (upper right). Cells are created for each set of four lines defining a pillar (lower left), and then the full grid is obtained (lower right).

disappears, and a representation of erosion surfaces is obtained with this procedure. If the collapse happens in some coordinate lines, the degenerate hexahedral cells may have at least five faces (Figures 2.3 and 2.4). Corner-point grid is a hexahedral grid and consequently should have six logical neighbors. In a stratigraphic reservoir model, a grid cell will only have a single top and bottom neighbor but may have various neighbors in all of the four lateral directions if any of the corresponding hexahedral faces are next to a fault (Figure 2.5). This procedure creates non-neighboring connections and nonmatching geometries in the primary ijk topology.

In this work, MRST was used as a grid processor of the input data, and this open-source software represents the corner-point grid as matching unstructured grids obtained by sectioning all nonmatching cell faces. For example, in realistic reservoir models, cells with non-neighboring connections across a fault plane will have more than six faces [33].

2.4. Setting of a corner point grid.

The public data sets used in this work are based on ECLIPSE [49] standard format. ECLIPSE does not allow to set the corners points in an arbitrary fashion, they are restricted with the following two parameters: coordinate lines and corner depths.

2.4.1. Coordinate Lines

A coordinate line is a straight non-horizontal line defined by two coordinates (x_1, y_1, z_1) and (x_2, y_2, z_2), where index 2 is more in-depth than index 1. The coordinate lines create a frame of lines; each line is identified by its index (i, j) and represent the lines where depth corners can set. With the depth of a grid block corner and the related coordinate line, the corner point's x and y coordinates are calculated. Excepting boundary cells, any coordinate line is correlated with four columns of cells and must be straight lines as cannot be horizontal.

2.4.2. Depth Points

The eight corner nodes delineate each grid cell. In each of the correlated cells, exactly two corners are on the coordinate line, one on the top face and bottom face, respectively. The corner nodes can move

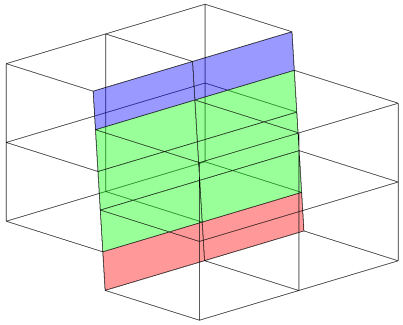

Figure 2.2: Fault faces. The faces marked in purple belong only to the cells behind the fault surface, the red faces belong only to the cells in front of the fault surface, and the green ones belong to cells on both sides.

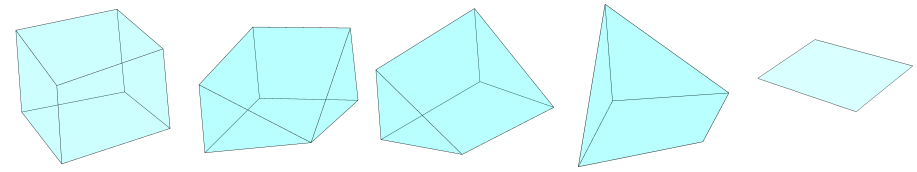

(a) Hexahedron (b) Heptahedron (c) Triangular prism (d) Pyramid (e) Polygon with zero volume

Figure 2.3: Degeneracy of corner point grids. All the geometries are variation of the hexahedron and but the rest have one or more pair of vertices with the same coordinates.

up and down on the coordinate line but are restricted to stay on it.

2.4.3. ECLIPSE Keywords

Coordinate lines and depth points are identified with the following ECLIPSE keywords:

COORD is the keyword used to describe the coordinate lines. As n_x and n_y are the number of cells in $x-$ and $y-$direction, the number of coordinate lines will be $n_x + 1$ and $n_y + 1$. ECLIPSE uses the book page format, so coordinate lines are then input line by line, and on each line, i going from 1 to $n_x + 1$.

ZCORN is the keyword used to describe the depths of each corner of each grid block. The intersection between a corner depth value and a coordinate line is unique so that all coordinates can be calculated from coordinate lines and corner depths. The number of corner depths will be $nx \times n_y \times n_z \times 8$.

Considering the book page format to define the corner cells, it starts firstly with the top northern edge of all cells, and they are read from west to east, then the southern edge. Once it is done, the first row of cells advances to the next one. After the top layer has been read, the bottom one is read with the same approach, and then go for the following layer.

ACTNUM is the keyword that represents the Boolean indicator. A value of 1 indicates that the consequent grid block is active, while a 0 implies that it is inactive.

2.5. Corner Point Grid Geometry

Compute cell centroids, cell volumes, face areas, face centroids, and face normals are straightforward for cartesian grids but are not the same for polyhedral grids as they may have curved polygonal faces. The following explanation of the procedure to obtain the cell geometry is based MSRT's approach: use of a tetrahedral subdivision [33].

Consider a face given by the points $\vec{p}(i_1), ..., \vec{p}(i_m)$ and let $\alpha = (\alpha_1, ..., \alpha_m)$ represent a multi-index that indicates how these points connect to form the outline of the faces.

MRST defines a so-called hinge point $\vec{p}_h$ to interpret the surface covered by the curved faces' node points. The hinge point is regularly provided in the grid's input description, but can also be computed

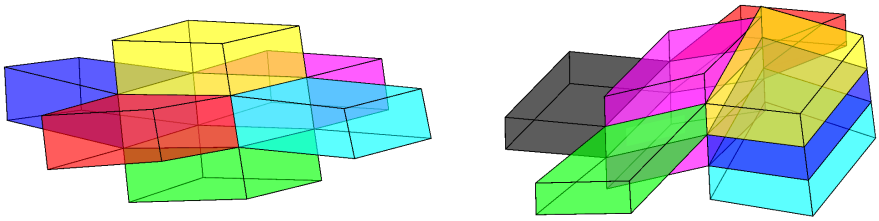

(a) Corner-point grid with six neighbors. (b) Corner-point grid with eight neighbors.

Figure 2.4: Local topology and geometry for a corner-point grid. The figure shows two cells from the Norne simulation model: (a) 27879 and (b) 11365.

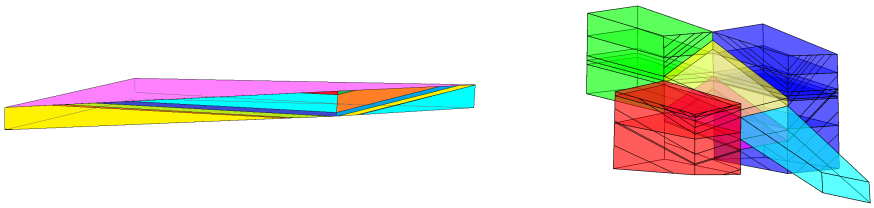

(a) Corner-point grid with six neighbors. (b) Corner-point grid with eight neighbors.

Figure 2.5: Complex geometry and topology, resulting in grid cells near faults in realistic reservoir models. The left figure shows a grid cell with two visible faces with six and seven neighbors, respectively. The right figure shows the same grid cell adjacent to fault faces. The cell has 19 unique faces.

as the center point of the m points that make up the face, $\vec{p}_h = \sum_{k=1}^{m} \frac{\vec{p}(\alpha_k)}{m}$.

The hinge point can be used to tessellate the face into m triangles. The triangles are specified by the points $\vec{p}(\alpha_k)$, $\vec{p}(\alpha_{mod(k,m)+1})$, and $\vec{p}_h$ for $k = 1, \ldots, m$. Each one of the triangles has a center point $\vec{p}_c^k$ defined as the average of its three vertexes and a normal vector and area given by

$$\vec{n}^k = (\vec{p}(\alpha_{mod(k,m)+1}) - \vec{p}(\alpha_k)) \times (\vec{p}_h - \vec{p}(\alpha_k)) = \vec{v}_1^k \times \vec{v}_2^k \tag{2.1}$$

$$A^k = \sqrt{\vec{n}^k \cdot \vec{n}^k} \tag{2.2}$$

The face area, centroid, and normal are computed with the following equations:

$$A_f = \sum_{k=1}^{m} A^k \tag{2.3}$$

$$\vec{c}_f = (A_f)^{-1} \sum_{k=1}^{m} \vec{p}_c^k A^k \tag{2.4}$$

$$\vec{n}_f = \sum_{k=1}^{m} \vec{n}^k \tag{2.5}$$

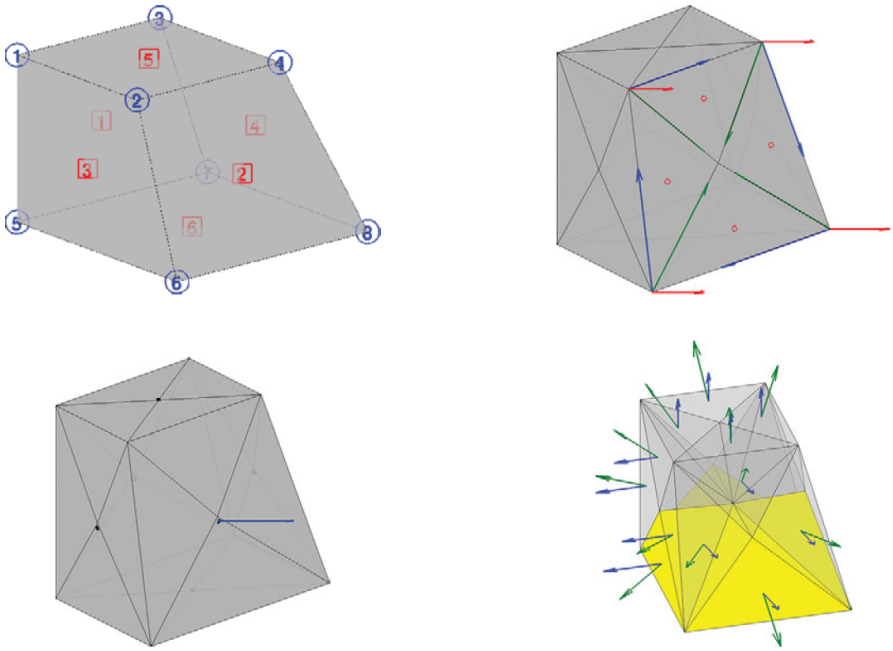

Figure 2.6: Computation of geometry data for a single corner-point cell using MRST. A corner-point cell with face numbers (squares) and node numbers (circles) (upper left). Tessellation of faces with vectors $\vec{v}_1^k$ (blue), $\vec{v}_2^k$ (green), and $\vec{n}^k$ (red) Uupper right). Face centroids and normal vectors calculated from tessellation (lower left). Triangulation of volume with vectors $\vec{c}_r^k$ (green) and $\vec{n}^k$ (blue) (lower right) (Source: MRST).

The centroid $\vec{c}_f$ does not match the hinge point $\vec{p}_h$ except if the planar face is a square.

To calculate the cell centroid and cell volume, first it is computed the center point $\vec{c}_c$ of the cell, defined as the average of the face centroids, $\vec{c}_c = \sum_{k=1}^{m_f} \frac{\vec{c}_f}{m_f}$, where m_f is the number of faces of the cell. The center point is connected to the m_t face triangles, and a unique triangulation of the cell volume is defined.For each tetrahedron, the vector $\vec{c}_r^k = \vec{p}_c^k - \vec{c}_c$ is defined and the compute the volume with:

$$V^k = \frac{1}{3}\vec{c}_r^k \cdot \vec{n}^k \tag{2.6}$$

Triangle normals $\vec{n}_k$ are modified to get a correct computation so that they point outward. Cell volume and cell centroid are defined with the following equations.

$$V = \sum_{k=1}^{m_t} V^k \tag{2.7}$$

$$\vec{c} = \vec{c}_c + \frac{3}{4V}\sum_{k=1}^{m_t} V^k \vec{c}_r^k \tag{2.8}$$

3

Project-based Embedded Discrete Fracture Model (pEDFM) formulation

This chapter reviews a mathematical model for multiphase flow in detail, and it introduces the final volume discretization in corner point grids for the resulting equations. A Fully Implicit (FIM) solver scheme is implemented in an open-source simulator and to obtain a coupled discrete system with two main unknowns: pressure and saturation.

3.1. Fine scale equations and solution strategy

3.1.1. Multiphase Flow

The mass conservation equations for the phases in a porous media are stated as:

$$\frac{\partial}{\partial t}(\phi\ \rho_\alpha\ S_\alpha) - \nabla \cdot (\rho_\alpha\ u_\alpha) = \rho_\alpha\ q \tag{3.1}$$

Where ϕ is porosity, while S_α, ρ_α, and u_α are saturation, density, and velocity of each phase α. q denotes the source and sink terms, e.g., well flow rates.

For incompressible flow, fluid and rock are considered do not change, so phi and rho are assumed to be constant over time. The previous assumptions lead to the resulting equation:

$$\phi \frac{\partial S_\alpha}{\partial t} + \nabla(u_\alpha) = q \tag{3.2}$$

Equation 3.2 represents a mass balance equation for incompressible fluid and rock. The phase velocities can be expressed using the multiphase extension of Darcy's Law:

$$u_\alpha = -\frac{1}{\mu_\alpha}\boldsymbol{K}(\nabla p) \tag{3.3}$$

Where $\boldsymbol{K}$ is permeability, μ_α is viscosity, and the main unknown, P is pressure. Gravity and capillary pressure are neglected, and the phase saturations are related through the saturation constraint ($\sum S_\alpha = 1$). The saturation constraint cancels out the accumulation term, and the following linear elliptic pressure equation is obtained:

$$-\nabla \cdot (\frac{1}{\mu_\alpha}\boldsymbol{K} \cdot \nabla p) = q \tag{3.4}$$

That serves a model pressure equation for incompressible fluids. The presented explanation is based on a general case, but in this work, fractures are considered as part of the domain, so the governing equations must be stated for both matrix and fractures.

3.1.2. Governing Equations

Once the grids for matrix and fracture are defined, the mass balance equations for multiphase fluid flow in porous media with n_{frac} discrete fractures for the rock matrix and for the lower dimensional fractures are stated as,

$$\frac{\partial}{\partial t}(\phi^m \rho_\alpha S_\alpha) - \nabla \cdot (\rho_\alpha \frac{1}{\mu_\alpha} \boldsymbol{K}^m \cdot \nabla p^m) = \rho_\alpha \, q^{mw} + \sum_{i=1}^{n_{frac}} \rho_\alpha^* \Psi^{mf_i} \quad \text{on} \quad \Omega_m \subseteq R^n \tag{3.5}$$

and

$$\frac{\partial}{\partial t}(\phi^{f_i} \rho_\alpha S_\alpha) - \nabla \cdot (\rho_\alpha \frac{1}{\mu_\alpha} \boldsymbol{K}^{f_i} \cdot \nabla p^{f_i}) = \rho_\alpha q^{f_i w} + \rho_\alpha^* \Psi^{f_i m} + \sum_{i=1}^{n_{frac}} (\rho_\alpha^* \Psi^{f_i f_j})_{j \neq i} \quad \text{on} \quad \Omega_f \subseteq R^{n-1} \quad \forall i \in \{1, \dots, n_{frac}\} \tag{3.6}$$

Here scripts m, f and w correspond to rock matrix, fractures and wells, respectively. q^{mw} and $q^{f_i w}$ are the source terms on matrix m and fracture f_i. Additionally Ψ^{mf_i}, and $\Psi^{f_i m}$ are the flux interactions terms between matrix m and overlapping fracture f_i corresponding to the grid cells where overlap occurs. $\Psi^{f_i f_j}$ is the flux exchange from j-th fracture to the i-th fracture on the intersecting elements. Mas conservation always holds, i.e., $\iiint_V \Psi^{mf_i} dV = -\iint_{A_{f_i}} \Psi^{f_i m} dA$, and $\iint_{A_{f_i}} \Psi^{f_i f_j} dA = -\iint_{A_{f_j}} \Psi^{f_j f_i} dA$.

The Peaceman well model is used to get the flux between the source terms (wells) and the reservoir:

$$q^{mw} = \frac{PI \cdot \lambda^* \cdot (p^w - p^m)}{\Delta V} \tag{3.7}$$

and fractures

$$q^{f_i m} = \frac{PI \cdot \lambda^* \cdot (p^w - p^{f_i})}{\Delta A} \tag{3.8}$$

where PI denotes the well productivity index, λ^* the effective mobility $\lambda = \frac{k}{\mu}$ between the well and the perforated grid cell. The control volumes ΔV and ΔA are utilized in the discrete system for the matrix, m, and fracture, f_i, respectively.

The flux interactions terms between matrix and fractures connectivities, Ψ^{mf_i} and $\Psi^{f_i m}$, and between fractures and fractures connectivities $\Psi^{f_i f_j}$, are defined through:

$$\Psi^{mf_i} = CI^{mf_i} \cdot \lambda^* \cdot (p^{f_i} - p^m) \tag{3.9}$$

$$\Psi^{f_i m} = CI^{f_i m} \cdot \lambda^* \cdot (p^m - p^{f_i}) \tag{3.10}$$

$$\Psi^{f_i f_j} = CI^{f_i f_j} \cdot \lambda^* \cdot (p^{f_j} - p^{f_i}) \tag{3.11}$$

where CI denotes the connectivity index between each two non-neighboring elements.

3.1.3. Finite volume discretization for corner point grids

Finite volume methods are conservative because they are derived from conservation of quantities over cell volumes, in other words, the flux entering a given cell volume is the same to that leaving the neighboring volume. To discretize the fluid flow problem, equation 3.4, it is used a standard finite-volume method with two-point flux approximation.

In finite-volume methods, the unknown quantities are represented in terms of average values defined over finite volumes and use this data to assemble approximations of the solution inside the cells.

Let the reservoir domain Ω^n in dimension n as a set of non-intersecting control volumes Ω_i. First, the equation 3.4 is rewritten in integral form using a single cell Ω_i as control volume:

$$\int_{\partial \Omega_i} \vec{u} \cdot \vec{n} dS = \int_{\Omega_i} q \, d\vec{x} \tag{3.12}$$

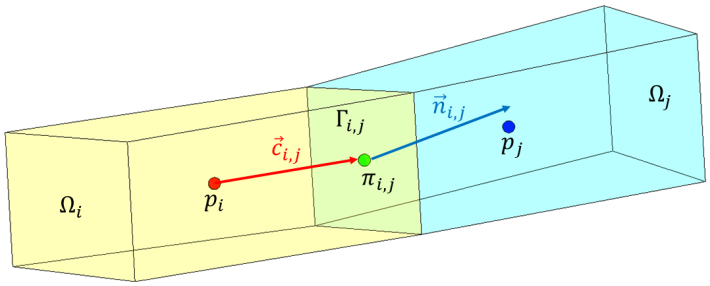

Figure 3.1: Two Point Flux Approximation (TPFA). Two neighbor cells are used to define the two-point flux discretization on polyhedral cells.

Use Darcy's law to compute the flux across two neighbouring cells i and j:

$$u_{i,j} = \int_{\Gamma_{i,j}} \vec{u} \cdot \vec{n} dS \tag{3.13}$$

The faces $\Gamma_{i,j}$ are denominated half face as they are linked with a grid cell Ω_i and a normal vector $\vec{n}_{i,i}$. It is assumed that the grid is matching to another one so that each interior half face will have a twin half face $\Gamma_{j,i}$ that also has an identical area $A_{i,j} = A_{j,i}$ but opposite normal vector $\vec{n}_{j,i} = -\vec{n}_{i,j}$.

The integral over the cell face is approximated by the midpoint rule, and Darcy's law, i.e.,

$$u_{i,j} \approx A_{i,j}(\boldsymbol{K}\, \Delta p)(\vec{x}_{i,j}) \cdot \vec{n}_{i,j} \tag{3.14}$$

where $\vec{x}_{i,j}$ indicates the centroid on $\Gamma_{i,j}$.

The one-sided finite difference is used to determine the pressure gradient as the difference between the pressure $\pi_{i,j}$ at the face centroid and the pressure at some point inside the cell. The reconstructed pressure value at the cell center is equal to the average pressure p_i inside the cell:

$$u_{i,j} \approx A_{i,j}\boldsymbol{K}_i \frac{(p_i - \pi_{i,j})\ \vec{c}_{j,i}}{|\vec{c}_{j,i}|^2} \cdot \vec{n}_{i,j} \longrightarrow u_{i,j} \approx T_{i,j}(p_i - \pi_{i,j}) \tag{3.15}$$

The vectors $\vec{c}_{j,i}$ are defined from cell centroids to face centroids. Face normals are assumed to have a length equal to the corresponding face areas: $A_{i,j} \cdot \vec{n}_{j,i}$.

$$T_{i,j} = A_{i,j}\boldsymbol{K}_i \frac{\vec{c}_{j,i}\vec{n}_{i,j}}{|\vec{c}_{j,i}|^2} \tag{3.16}$$

The one-sided transmissibilities $T_{i,j}$ are related to a single cell and provide a two-point relation between the flux across a cell face and the pressure difference between the cell and face centroids. The proper name for these one-sided transmissibilities is half-transmissibilities as they are associated with a half face.

Finally, a continuity of fluxes across all faces, $u_{i,j} = -u_{j,i}$ and continuity of face pressures $\pi_{i,j} = \pi_{j,i} = \pi_{ij}$ are set and the following equations are obtained,

$$T_{i,j}^{-1}\, u_{ij} = p_i - \pi_{ij} \tag{3.17}$$

$$-\,T_{j,i}^{-1}\, u_{ij} = p_j - \pi_{ij} \tag{3.18}$$

interface pressure π_{ij} is eliminated and the two-point flux approximation (TPFA) scheme is defined as,

$$u_{ij} = T_{ij}\ (p_i - p_j) \tag{3.19}$$

$T_{ij}$is the transmissibility associated with the connection between two cells, Ω_i and Ω_j.

$$T_{ij} = [T_{i,j}^{-1} + T_{j,i}^{-1}]^{-1} = \frac{T_{i,j}\, T_{j,i}}{T_{i,j} + T_{j,i}} \tag{3.20}$$

The TPFA scheme uses two ”points”, the cell averages p_i and p_j, to approximate the flux across the interface $\Gamma_{i,j}$ between cells Ω_i and Ω_j.

3.1.4. Fine-scale discrete system

The coupled system of non-linear equations with two main unknowns (p, T) described in Section 3.1.2, i.e., (Eqs. 3.5 - 3.11) is discretized spatially utilizing the two-point-flux-approximation (TPFA) scheme and temporally with a backward Euler scheme (implicit) [5]. The discretization provides a set of structured grids for a 3D porous medium with 2D fracture planes generated independently. The resulting non-linear FIM system is solved by applying the Newton-Raphson iterative method [5].

The mass flux between two neighboring grid cell volumes i and j applying TPFA scheme can be formulated as,

$$F_{ij} = -\frac{\overset{*}{\rho_\alpha}}{\overset{*}{\mu_\alpha}} T_{ij}(p_i - p_j) \tag{3.21}$$

where$T_{ij} = \frac{A_{ij}}{d_{ij}} K_{ij}^H$ represents the transmisibility between grid cells i and j. A_{ij} is the interface area between the grid cells, d_{ij} is the distance between their cell centers and K_{ij}^H is the harmonic average of the grid cell permeabilities define at the interface of grid cells i and j.

The superscript $*$ in the fluid properties are obtained using the upwind scheme. It take as reference the fluid velocity at the cell interfaces to choose the right cell with its linked fluid properties: density and viscosity. If $u_{i,j}$ > 0, for instance, velocity is positive and assumed that propagates it from left to right, and hence it is used the flux from the left side of the cell interface to update the fluid properties data. If the flux $u_{i,j}$ is negative in a different scenario, the mass flux is continually flowing from cell j into cell i, and it is thus natural to choose cell i.

For the matrix-fracture or fracture-fracture connectivities, the mass flux between two non-neighboring grid cells i and j is found through EDFM formulation [18] [50].

The mass flux between a matrix (m) cell i and a fracture (f) cell j can be also specified as,

$$\mathcal{F}_{ij}^{mf} = -\mathcal{F}_{ij}^{fm} = -\frac{\overset{*}{\rho_\alpha}}{\overset{*}{\mu_\alpha}} T_{ij}^{mf}(p_i^m - p_j^f) \tag{3.22}$$

where T_{ij}^{mf} denotes the transmissibility, that is defined as,

$$T_{ij}^{mf} = K_{ij}^H CI_{ij} \tag{3.23}$$

CI_{ij} is the connectivity index between the intersecting cell matrix and the fracture element, and K_{ij}^H is the harmonically averaged permeability between them.

The EDFM represents the matrix-fracture connectivity index as,

$$CI_{ij} = \frac{A_{ij}^{mf}}{\langle d \rangle_{ij}} \tag{3.24}$$

where A_{ij}^{mf} is the surface area of fracture cell j overlapping matrix cell i, and $\langle d \rangle_{ij}$ is the average distance between these cells [18], that can be computed as,

$$\langle d \rangle_{ij} = \frac{1}{V_i} \int_{V_i} x_n(x) dV_i \tag{3.25}$$

where x_n is the unit normal vector pointing to fracture face j, x is the distance from the fracture, and V and dV are the volume and volume element of the grid cell i. The integral is approximated with a numerical integral that is calculated through the use of equidistant points. This approach is chosen to simplify the extension of the integral to calculate $\langle d \rangle$ because of the complexity of fractures' geometrical position in a realistic fracture set.

The mass flux exchange among two intersecting fracture elements i (on fracture f) and j (on fracture g) is denoted as,

$$\mathcal{F}_{ij}^{fg} = -\mathcal{F}_{ij}^{fg} = -\frac{\rho_\alpha^*}{\mu_\alpha^*} T_{ij}^{fg} (p_i^f - p_j^g) \tag{3.26}$$

where T_{ij}^{fg} represents the transmissibility between the two cells obtained through a lower-dimensional connectivity index formulation. The intersection of 2D fracture plates is a 1D line, and for 1D fracture line-segments, the intersection is a point. The intersection forms a line segment I_{ij} with the average distances from the intersection segment of $\langle d \rangle_{iI_{ij}}^f \neq \langle d \rangle_{jI_{ij}}^g$. Hence, T_{ij}^{fg} is given with a harmonic-average formulation, i.e.,

$$T_{ij}^{fg} = K_{ij}^H \frac{CI_{iI_{ij}}^f \times CI_{jI_{ij}}^g}{CI_{iI_{ij}}^f + CI_{jI_{ij}}^g} \tag{3.27}$$

where, e.g., $CI_{iI_{ij}}^f$ represents the connectivity index between the 2D fracture element i and the 1D intersection line segment I_{ij}.

The fine scale discrete mass balance equation at each time step reads

$$\frac{(\phi^m \rho_\alpha S_\alpha)_i^{n+1} - (\phi^m \rho_\alpha S_\alpha)_i^n}{\delta t} + \sum_{j=1}^{N_n} F_{ij} + \sum_{k=1}^{n_{frac}} \left(\sum_{j=1}^{N_{f_k}} \mathcal{F}_{ij}^{mf_k} \right) = (\rho_\alpha q^{mw})_i \quad , \quad \forall i \in \{1, \dots, N_m\} \tag{3.28}$$

for the element i in matrix m and

$$\frac{(\phi^{f_h} \rho_\alpha S_\alpha)_i^{n+1} - (\phi^{f_h} \rho_\alpha S_\alpha)_i^n}{\delta t} + \sum_{j=1}^{N_n} F_{ij} + \sum_{j=1}^{N_m} \mathcal{F}_{ij}^{f_h m} + \sum_{k=1}^{n_{frac}} \left(\sum_{j=1}^{N_{f_k}} \mathcal{F}_{ij}^{f_h f_k} \right) = (\rho_\alpha q^{f_h w})_i \quad , \quad \forall i \in \{1, \dots, N_{f_h}\} \tag{3.29}$$

for the element i in fracture f_h. N_m and N_{f_k} represent the number of elements in matrix m and fracture f_k respectively. N_m is the number of neighboring grid cells.

A fully implicit scheme is selected to solve all the pressure-dependent and saturation-dependent terms [20] [21]. The fully implicit discretization is unconditionally stable because there is no stability condition (CFL condition) that restrain the size of the time step. The residual of the mass balance equations 3.28 and 3.29 can be written as subtracting the left-hand side from the right-hand side in each equation. The residual of the mass balance equation for the matrix reads,

$$(r_\alpha^m)^{n+1} = \rho_\alpha q^{mw} - \frac{(\phi^m \rho_\alpha S_\alpha)_i^{n+1} - (\phi^m \rho_\alpha S_\alpha)_i^n}{\Delta t} - \sum_{j=1}^{N_n} F_{ij} - \sum_{k=1}^{n_{frac}} \left(\sum_{j=1}^{N_{f_k}} \mathcal{F}_{ij}^{mf_k} \right) = 0 \quad \forall i \in \{1, \dots, N_{f_m}\} \tag{3.30}$$

for the rock matrix, and

$$(r_\alpha^{f_h})^{n+1} = \rho_\alpha q^{f_h w} - \frac{(\phi^{f_h} \rho_\alpha S_\alpha)_i^{n+1} - (\phi^{f_h} \rho_\alpha S_\alpha)_i^n}{\delta t} - \sum_{j=1}^{N_n} F_{ij} - \sum_{j=1}^{N_m} \mathcal{F}_{ij}^{f_h m} - \sum_{k=1}^{n_{frac}} \left(\sum_{j=1}^{N_{f_k}} \mathcal{F}_{ij}^{f_h f_k} \right) = (\rho_\alpha q^{f_h w})_i \quad , \quad \forall i \in \{1, \dots, N_{f_h}\} \tag{3.31}$$

for fracture f_h. The full residual vector at time-step n is obtained by a vertical concatenation of both residuals.

$$r^n = [(r^m)^n, (r^{f_1})^n, \dots, (r^{f_{n_{frac}}})^n]^T \tag{3.32}$$

Likewise, p^n and S^n indicate the vectors of pressure and saturation unknowns (matrix and fractures). The residual at time step $n+1$, r^{n+1} is a non-linear function of p^{n+1} and S^{n+1}, it needs to be solved by using a Newton-Raphson method at each time step. It is expressed as,

$$r^{\nu+1} = r^{\nu} + \frac{\partial r}{\partial p}|^{\nu}\delta p^{\nu+1} + \frac{\partial r}{\partial S_{\alpha}}|^{\nu}\delta S_{\alpha}^{\nu+1} \tag{3.33}$$

where, ν represents the iteration index. At each iteration, the linearized system of equation is written as $J^{\nu}\delta x^{\nu+1} = -r^{\nu}$. J^{ν} is the Jacobian matrix including all the derivatives and $\delta x = [\delta p, \delta S]^T$ is the vector of unknowns. For a two-phase system (w indicates water and o oil) with pressure (p) and saturation (S) with main unknowns, the linear system states as:

$$\underbrace{\begin{bmatrix} J_{op}^{mm} & J_{op}^{mf} & J_{oS}^{mm} & J_{oS}^{mf} \\ J_{op}^{fm} & J_{op}^{ff} & J_{oS}^{fm} & J_{oS}^{ff} \\ J_{wp}^{mm} & J_{wp}^{mf} & J_{wS}^{mm} & J_{wS}^{mf} \\ J_{wp}^{fm} & J_{wp}^{ff} & J_{wS}^{fm} & J_{wS}^{ff} \end{bmatrix}^{\nu}}_{J_0^{\nu}} \underbrace{\begin{bmatrix} \delta p^m \\ \delta p^f \\ \delta S_w^m \\ \delta S_w^f \end{bmatrix}^{\nu+1}}_{\delta x_0^{\nu+1}} = \underbrace{\begin{bmatrix} r_o^m \\ r_o^f \\ r_w^m \\ r_w^f \end{bmatrix}^{\nu}}_{r_0^{\nu}} \tag{3.34}$$

To obtain a converged solution, the following conditions have to established:

$$\|r\|_{\infty} < \epsilon_1 \quad \wedge \quad \frac{\|\delta p\|_{\infty}}{\|p\|_{\infty}} < \epsilon_2 \quad \wedge \quad \|\delta p\|_{\infty} < \epsilon_2 \tag{3.35}$$

Here, each threshold (ϵ_1, ϵ_2) is a tolerance defined by the user as input at the beginning of the simulation.

3.2. Project-based Embedded Discrete Fracture Model Implementation

3.2.1. Embedded Discrete Fracture Model (EDFM)

The EDFM (Embedded Discrete Fracture Modeling) method split a fractured medium into an individual mesh for the matrix and fractures and couple them through flux interactions. EDFM differs from DFM since fractures do not need to be restricted to be placed between grid cells. The fractures in EDFM are characterized as a lower dimensional object. The EDFM concept for a 2D reservoir - 1D fracture is visualized in the figure 3.2.

For realistic field scenarios with several and complex fractures networks it can be practical if it is possible to get rid of the limitation of mesh conformity. EDFM splits a fractured medium into a separate fracture and matrix mesh, and to connect them via a transfer function.

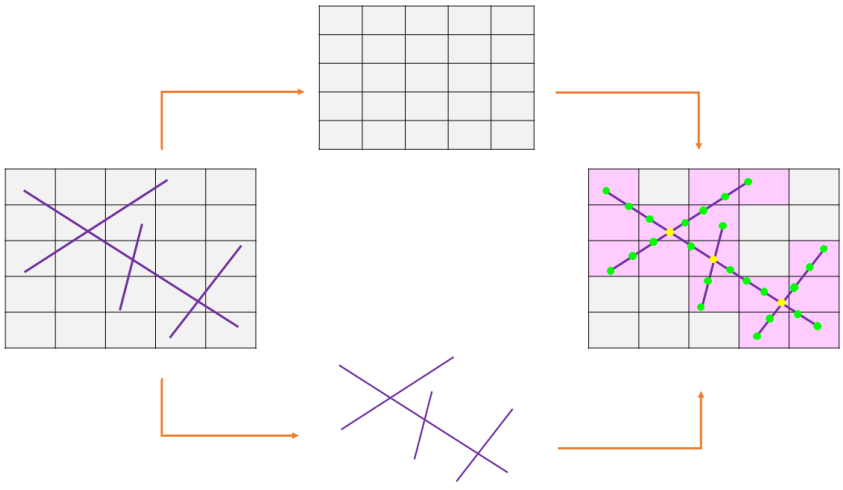

Figure 3.2: EDFM concept. The fractured media (left) is independently divide into a matrix grid system (upper center) and a fracture network grid (lower center). The matrix and fracture grids are displayed together (right) with intersected matrix cells highlighted.

The three sorts of connection are provided by EDFM for the mass flux terms, they are as follows:

- between the matrix block and a fracture segment.
- between fracture segments of a fracture.
- between intersecting fracture segments.

EDFM [18] [32] establish the fracture (f - cell matrix (i) transmissibility as,

$$T_{if} = \frac{2A_{if}}{\langle d \rangle_{if}} \lambda_{if} \tag{3.36}$$

where A_{if} is the surface area that is twice the area A_{if} since a fracture has two sides. λ_{if} is the effective transmissibility. The cell-matrix - cell-matrix connections related to the cell neighbors (j and k) remains the same as they are defined through TPFA finite volume scheme:

$$T_{ij} = \frac{A_{ij}}{\Delta x} \lambda_{ij} \qquad T_{ik} = \frac{A_{ik}}{\Delta y} \lambda_{ik}. \tag{3.37}$$

3.2.2. Project-based Embedded Discrete Fracture Model (pEDFM)

The presence of parallel transmissibilities limits the effectiveness of the EDFM approach since the method fails to represent flow barriers (fractures with permeability below the matrix permeability values). pEDFM [50] [27] [20] is a novel approach that resolves the limitations of EDFM since it removes that parallel transmissibilities. This advantage allows modeling fractures any conductivity contrast with respect to the matrix. pEDFM fixes the EDFM limitation with the introduction of additional fracture – matrix connections, in addition to modifications in matrix-matrix and fracture-fracture connectivities in the intersecting regions.

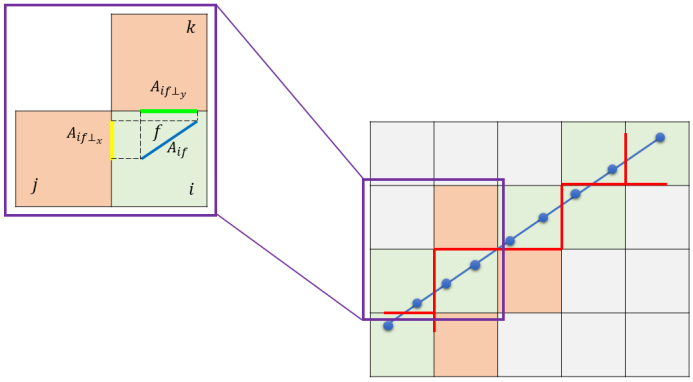

Figure 3.3: pEDFM illustration for a 1D fracture intersected on a 2D structured grid matrix. The intersected matrix cells are highlighted in green color. The cells highlighted in orange have a role in the definition of the additional non-neighbouring connections between matrix grid cells and fractures.

Firstly, it is detected all the connectivities between two adjacent cells separated because of the overlying fractures. A geometric procedure is used to establish a continuous projection path for each one of the fracture networks on the matrix domain. The implementation developed identifies the interfaces in neighboring connections and disconnects them, so the flow sequence is forced to occur in one route: matrix – fracture – matrix.

Figure 3.3 illustrate the connection transmissibility for pEDFM for a 2D case. A fracture element f being partially overlapped the matrix grid cell i, which has two neighbors matrix cells j and k. A_{if} represents the area of the fracture segment, and projections are defined on the interface between the intersected matrix grid cell i and its neighboring grid cells j and k. In the 3D case, it includes an additional projection. The projected faces act as the reference to define the extended fracture – matrix connections. For each one of the dimensions, the projection area fractions are defined through:

$$A_{if\perp x_e} = A_{if} \times cos(\gamma), \qquad x_e \in x, y, z \tag{3.38}$$

Where γ is the angle between the fracture element and the projected face area in the related dimension, the fracture segment projection on the interface connecting matrix grid cell i and j. Transmisibilities are specified to link the fracture element f to each non-neighboring matrix grid cells j and k:

$$T_{i_ef} = \frac{A_{if\perp x_e}}{\langle d \rangle_{i_ef}} \Lambda_{i_ef}, \qquad x_e \in x, y, z \tag{3.39}$$

Where $\langle d \rangle_{i_ef}$ is the average distance between the fracture element f and matrix grid cell $i_e|$, and Λ_{i_ef} is the effective fluid mobility between the non-neighboring cells.

In addition to the extra fracture – matrix connections, the matrix-matrix connections must be modified correspondingly since the fracture is blocked some parts of the matrix flow area.

$$T_{ii_e} = \frac{A_{ii_e} - A_{if\perp x_e}}{\Delta x_e} \Lambda_{i_ef}, \qquad x_e \in x, y, z \tag{3.40}$$

Where A_{ii_e} is the area of the interface shared by matrix cells i and j. To simplify the calculations, the modified transmissibilities are obtained by multiplication of coefficient α that is defined as a ratio of the projected cross-section area and the consequent face's cross-section area. If the fracture cuts through the entire matrix cell, the projection will cover the entire interface, then α is 1.0. This approach results in zero transmissibility between the neighboring matrix grid cells, therefore removing the parallel transmissibilities.

4

Test Cases: Data Sets

In this work, it has been used five public data sets of reservoir models based on corner point grid geometry: the Johansen Formation, the SAIGUP Model, the Brugge Model, the Norne Field, and the Volve Field. The data sets are available for the public in general and can be downloaded through MSRT or request it to TNO (Brugge Model).

4.1. ECLIPSE Keywords

The data set available are in ECLIPSE standard format, so the following ECLIPSE keywords are identified in the data to obtain the rock parameters:

PORO: It identifies the porosity values, and every grid block has a non-negative real number value that characterizes the rock property.

PERMX / PERMY / PERMZ: They recognize the permeability data in the $x-$, $y-$, and $z-$direction, and every grid of the model has a non-negative real number value that represents the parameter.

NTG: It identifies the net gross ratio values and they are used to change from gross to net thicknesses. Similarly, they are represented with a non-negative real number for every grid block.

MULTX / MULTY / MULTZ: They specify the transmissibility multipliers in $x-$, $y-$ and $z-$direction, and they are represented with a non-negative real number for every grid block. They take values between zero and one and are used to modify the effective transmissibility between a cell (i, j, k) and the cell immediately above $(i, j, k + 1)$ in the case of MULTZ (vertical multiplier). MULTX and MULTY (horizontal multipliers) play an analogous function for vertical faces.

SATNUM: It identifies the saturation function region numbers; in other words, the different rock types present in the reservoir model.

4.2. The Johansen Formation

The water-bearing Johansen formation was a potential candidate for CO_2 stored in a project promoted by the Norwegian government. The Norwegian continental margin owns excellent potential for CO_2 storage options in saline aquifers.

The Johansen formation [12] is located in the deeper part of the Sognefjord delta, 40–90 km offshore Mongstad on Norway's southwestern coast. It belongs to the Lower Jurassic Dunlin group and is interpreted as a laterally extensive sandstone, and it is overlaid by the Dunlin shale and below by the Amundsen shale. A saline aquifer is placed in-depth levels ranging from 2200m to 3100m below sea level. The depth levels make the formation ideal for CO_2 storage due to the pressure regimes existent in the field (CO_2 be in the supercritical phase).

These three formations have uniquely different permeabilities and perform very different roles in the CO_2 sequestration process. The Johansen sandstone has relatively high porosity and permeability, and it is suitable as a container to keep the CO_2. The low-permeability overlaying Dunlin shale plays a seal that avoids the CO_2 from leaking to the sea bottom.

The Johansen Formation has an average thickness of nearly 100 m, and the water-bearing extends laterally up to 60 km in the east-west direction and 100 km in the north-south direction. The aquifer has

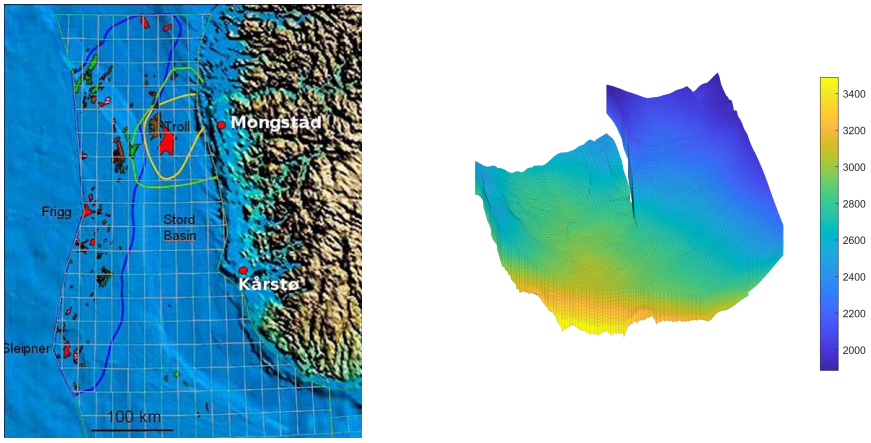

Figure 4.1: Location of the Johansen formation. It is contained within the green curve, and the yellow curve represents areas where seismic is known (courtesy of Gassnova). Depth map of the Johansen model ("NPD5" data set).

good sand quality with average porosities of roughly 25%; this implies that the Johansen formation's theoretical storage capacity can exceed one gigatonne of CO_2 if accounts and residual brine saturation (about 20%). The northwestern parts of the Johansen Formation are located some 500 m below the operating Troll field, one of the North Sea's largest hydrocarbon fields.

4.2.1. Rock properties

The Johansen sandstone is a structure with a wedge shape pinched out in the front part of the model and divided into two sections at the back. 4.3(b) shows the porosity of the model, and 4.3(b) shows the cells with porosity values larger than 0.1 that belongs to Johansen formation. The permeability tensor is diagonal, with the vertical permeability equivalent to one-tenth of the horizontal permeability. Figure 4.3 shows two different plots of the permeability of the model. The left graph presents the permeability of the whole model. In the right graph, it has been excluded the Dunlin shale above Johansen and the Amundsen shale below and illustrates the Johansen sandstone's permeability. In both graphs, the permeability is represented in a logarithmic color scale.

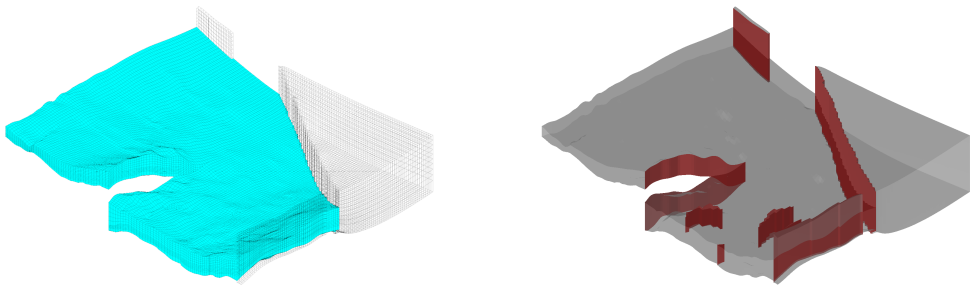

Figure 4.2: Display of the Johansen model ("NPD5" data set). The left graph represents the active section (colored) of the model, and the right figure shows the faults marked with red color.

4.2.2. Data Set

The MatMoRA project has created five models of the Johansen formation: one full-field model (149 × 189 × 16 grids), three homogeneous sector models (100 × 100 × n for n = 11,16,21), and one heterogeneous sector model (100 × 100 × 11). In this work, it has been consider the last data set.

In the reservoir field model, the Johansen formation is represented by five layers of cells. The Amundsen shale below the Johansen formation and the low-permeable Dunlin shale above are characterized by one and five cell layers, respectively. The Johansen formation consists of approximately 80% sandstone and 20% claystone, whereas the Amundsen formation consists of siltstones and shales,

and the Dunlin group has high clay and silt content.

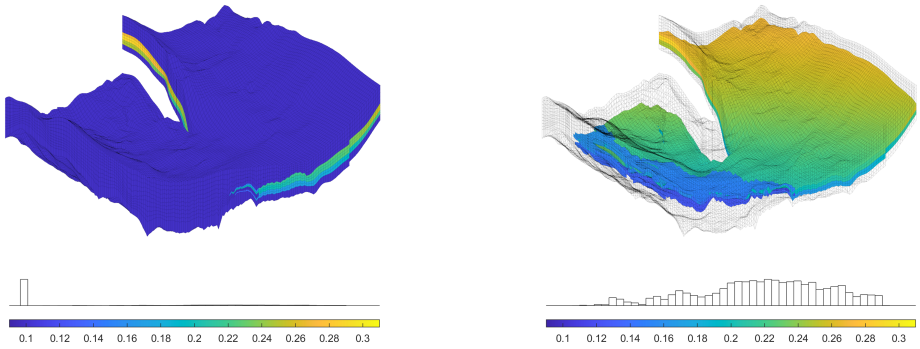

(a) Whole model porosity (b) Johansen formation porosity

Figure 4.3: Porosity for the Johansen model ("NPD5" data set). The left figure shows porosity for the whole model, whereas the right figure shows the porosity of the Johansen formation (sandstone).

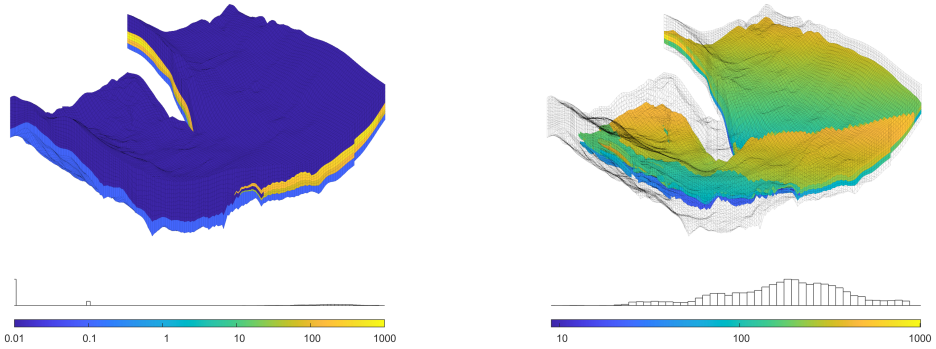

(a) Whole model porosity (b) Johansen formation porosity

Figure 4.4: Permeability of the Johansen model ("NPD5" data set). The left graph shows the permeability of the whole model, whereas the right plot only shows the permeability of the Johansen sandstone.

4.3. SAIGUP Model

SAIGUP is an acronym for Sensitivity Analysis of the Impact of Geological Uncertainties on Production forecasting in clastic hydrocarbon reservoirs. The SAIGUP modeling project evaluated the impact of geological factors on production in an extensive suite of synthetic shallow-marine reservoir models [39].

The SAIGUP project focuses on shoreface reservoirs in which the sediment deposition is due to the variation of the sea level. Faults and geological horizons surrounding a shoreface petroleum reservoir, and within it, it is common to find faults and flow barriers. Geological features and petrophysics are considered in reservoir modeling to accurately estimate the reservoir volume and establish the best well pattern to maximize its production.

Facies modeling allows us to separate facies whose flow properties differ considerably, and the flow properties have an essential role in estimating the reservoir's production capacity. The SAIGUP reservoir was divided into four zones to model the five facies. Horizontal flat barriers were included between the zones to represent a decrease in vertical communication.

4.3.1. Rock properties

The permeability is represented through an anisotropic tensor with zero vertical permeability in several cells. The horizontal and vertical permeabilities are shown in figure 4.7. A low permeability region along the reservoir's top structure is presented since a high shale content is present, and high-permeable sand bodies cross that low-permeable layers. The net-to-gross parameter provides a correlation that is presented between the permeabilities with the sand content.

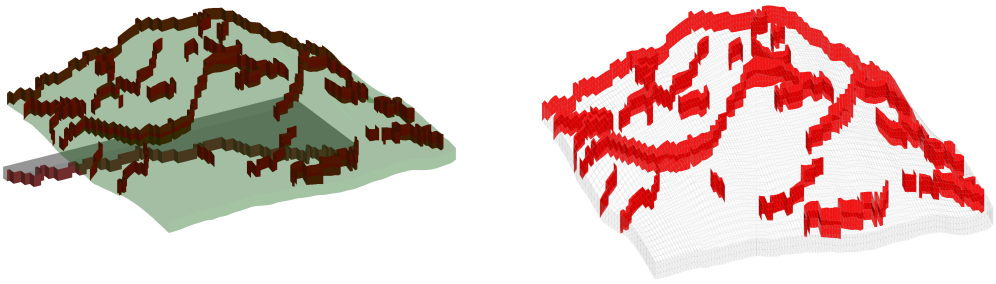

Figure 4.5: Display of the SAIGUP Model. The left graph represents the active section (colored) of the model, and the right figure shows the faults marked with red color.

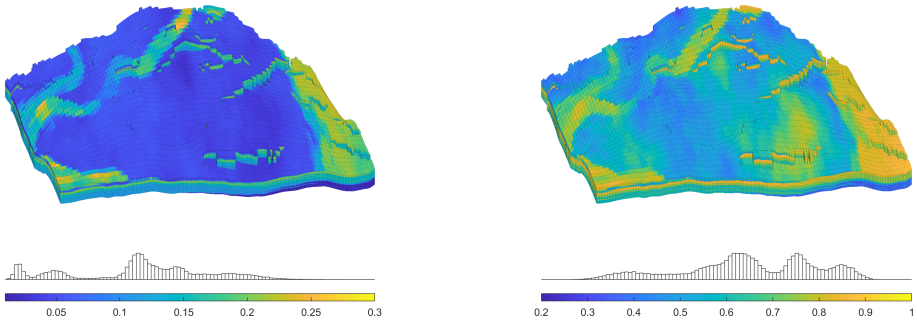

Figure 4.6: Porosity and N/G for the SAIGUP model. The left graph shows the porosity mapped in the structural model, and the right picture shows net-to-gross.

The porosity and horizontal permeability distributions are multi-modal since five different modes can be recognized related to the five different petrophysical modeling facies.

The SAIGUP model has six user-defined rock types that are also known as saturation regions. They are used to indicate distinct rock fluid properties such as relative permeability and capillary pressure functions.

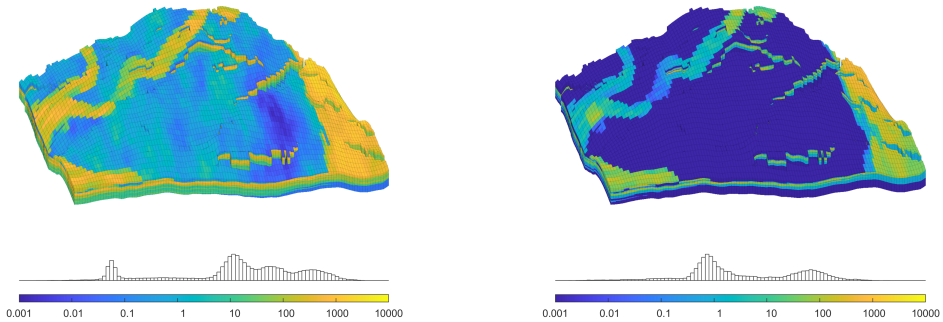

Figure 4.7: Permeability for the SAIGUP model. The left figure plot shows the horizontal permeability and vertical permeability in the right one. Both figures are plotted using a logarithmic color scale.

4.3.2. Data set

The artificial reservoirs were generated based on how shoreface depositions are carried on. SAIGUP project produced a broad set of geostatistical realizations and structural models to characterize a broad range of shallow-marine sedimentological reservoirs. All models are synthetic, but they contain structural and stratigraphic complex features existing clastic reservoirs. The realization used in this work is

publicly available in MRST.

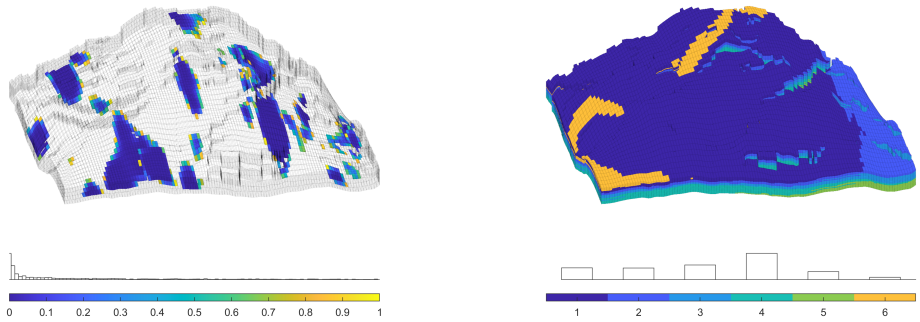

Figure 4.8: Vertical multipliers and saturation regions of the SAIGUP model. The left graph shows the areas of the reservoir where vertical multiplier models a reduction in perpendicular communication. The right picture shows the rock type distribution for SAIGUP model; the color bar shows the six rock types.

4.4. Brugge Model

The Brugge model is an SPE benchmark study conceived as a reference platform to assess different closed-loop reservoir management methods [44]. It is the largest and most complex test case on closed-loop optimization to represent real field management scenarios.

The active Brugge field model has 44550 corner point grid cells, and the main geological features present in the model are a boundary fault and an internal fault. Seven different rock regions with their particular petrophysical properties are distributed in the whole model. Thirty wells are included in the field model's well production pattern: 20 producers and ten injectors.

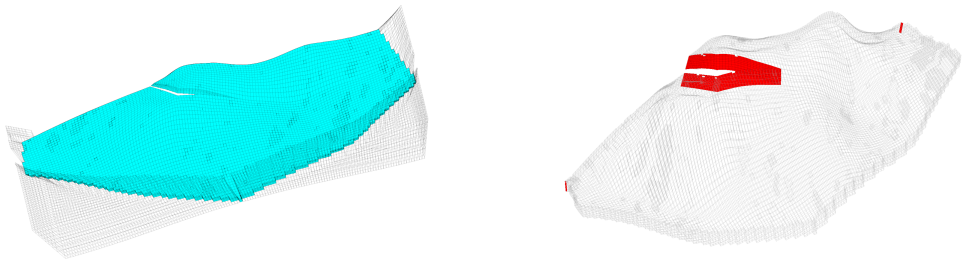

(a) Whole model (b) Faults present in the model

Figure 4.9: Display of the Brugge model. The left graph represents the active section (colored) of the model, and the right figure shows the faults marked with red color.

4.4.1. Geological Model

The geological structure of the Brugge Field contains an east/west elongated half-dome with a boundary fault at its northern edge and an internal fault with a throw at an angle of nearly 20 degrees to the northern fault edge. The dimensions of the field are approximately 10 × 3 km. The original high-resolution model is 20 million grid cells, with average cell dimensions 50 × 50 × 0.25 m. In addition to the essential petrophysical properties for reservoir simulation (sedimentary facies, porosity, permeability, net-to-gross, and water saturation), the grid model includes properties measured in real fields (gamma-ray, sonic, bulk density, and neutron porosity). The data were generated at a detailed scale to produce reliable well log data in the thirty wells drilled in the field.

The original high-resolution model was upscaled to a 450000 grid cell model, which established the foundation for all additional reservoir simulations of the reference case. A set of 104 realizations, in which each one of them contains 60000 grid cells, was created from the data extracted from the reference case.

All the realizations used the same geological structure of the field. The North Sea Brent-type field

was the reference to generate the reservoir zones' rock properties and thicknesses. An alteration of the formations' vertical sequence for the general Brent stratigraphy column (comprising the Broom-Rannoch-Etive-Ness-Tarbert Formations) was made and resulted in that the highly permeable reservoir zone switched locations with the underlying area (less permeable and heterogeneous).

4.4.2. Rock properties

A reservoir model with 60000 grid cells was the reference to create 104 upscaled realizations for the reservoir properties. The properties that contain the realizations are facies, porosity, a diagonal permeability tensor, net-to-gross ratio, and water saturation.

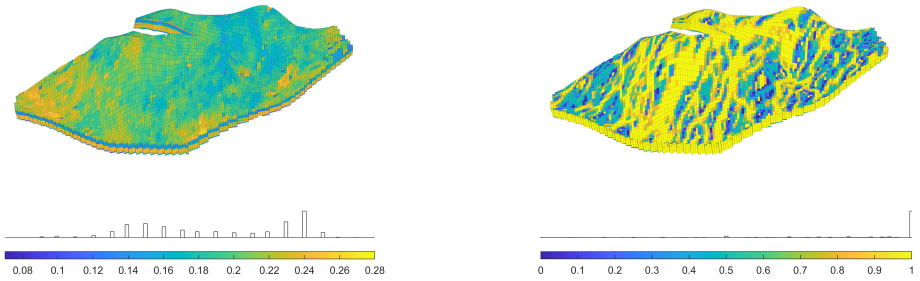

Figure 4.10: Porosity and N/G for the Brugge model. The left graph shows the porosity of the model, and the right one shows net-to-gross mapped in the structural model.

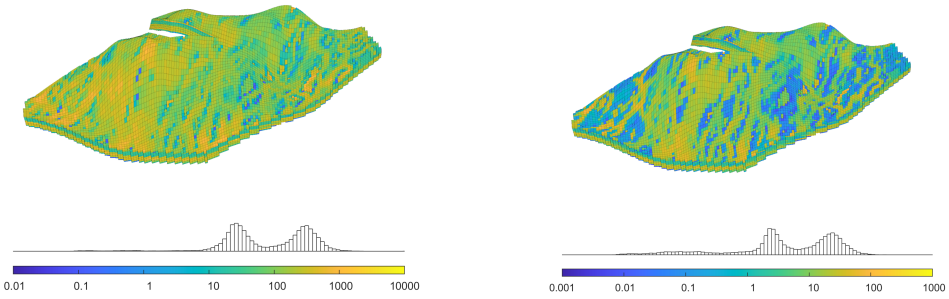

Figure 4.11: Permeability map of the Brugge model. The left figure shows the horizontal permeability, and the right figure shows vertical permeability; both are plotted using a logarithmic color scale.

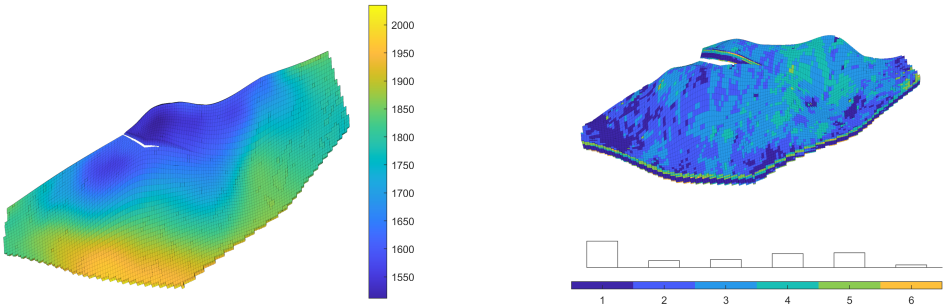

Figure 4.12: Depth map and saturation regions of the Brugge field. The left graph shows the depth map, and the right graph shows the rock type distribution displayed in the color bar.

4.5. Norne Field

Norne ([52]) is an oil and gas field situated in the Norwegian Sea around 80 kilometers north of the Heidrun oil field. The field dimensions are approximately 9 × 3 km and the seawater depth in the area

is 380 meters. The field is placed in a license awarded in 1986 and incorporates blocks 6608/10 and 6608/11. Equinor is the current field operator. The expected oil recovery factor is more than 60%, which is very high for an offshore subsea oil reservoir.

Subsurface data from the Norne field have been published for research and education purposes thanks to NTNU, Equinor, and partners' initiative. The full simulation mode can be obtained through the Open-Porous-Media (OPM) project (opm-project.org) [43]. The Norne field simulation model was the first benchmark case based on real field data available to the public. The model is based on the 2004 geological model and consists of 46 × 112 × 22 corner-point grid cells.

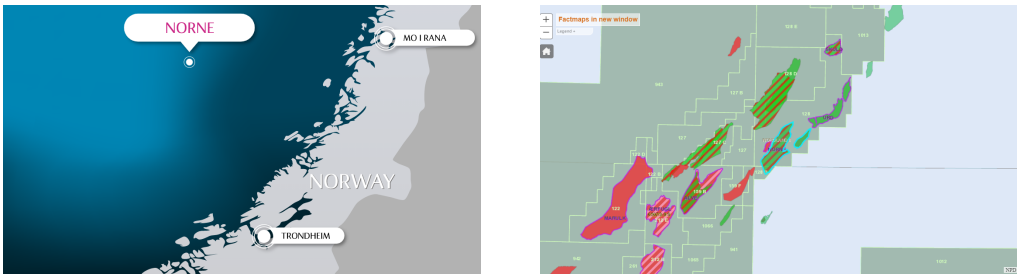

Figure 4.13: Location of the Norne Field. The left plot shows the field located in the Norwegian sea (source: Equinor), and the right picture shows the location of the licensed blocks (source Norwegian Petroleum Directorate).

4.5.1. Reservoir

The Oil and gas production of Norne is obtained from a Jurassic sandstone, which lies at a depth of 2500 meters below sea level. The original estimation of recoverable resources was 95.2 million m3 for oil, mainly in the Ile and Tofte formations, and 13.01 billion m3 for gas in the Garn formation.

4.5.2. Field Development

The Alve field finding preceded the Norne field's discovery in 1992. The plan for development and operation (PDO) was approved in 1995, and the production started in 1997. The field development infrastructure consists of production, storage, and offloading vessel (FPSO) attached to subsea templates. Water injection is the drive mechanism to produce the field. Since 2001, the gas has been exported from Norne, but in 2005 the gas injection stopped as planned to be exported.

In 2019, Norne FPSO was granted a lifetime extension to increase value creation from the Norne field and its satellite fields, and also, the blowdown of the gas cap in the Not Formation started. In 2020 two production wells are planned to be drilled in the Ile Formation.

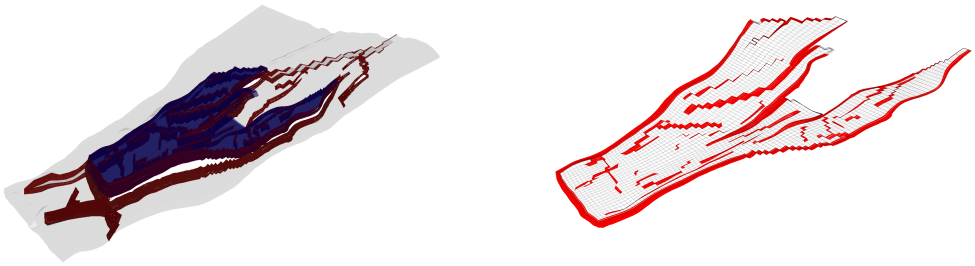

Figure 4.14: Display of the Norne field model. The left graph represents the active section (colored) of the model, and the right figure shows the faults marked with red color.

4.5.3. Petrophysical Data

The field simulation model's petrophysical data consist of porosity, permeability, net-to-gross, and transmissibility multiplier data. Permeability is anisotropic and heterogeneous, with a clear layered structure as expected for a real reservoir field model. The vertical communication is decreased in significant regions of the model by the transmissibility multiplier data available, resulting in intermediate layers of the reservoir with values close to zero. The field's porosity values are in the interval between

0.094 and 0.347, and a reduction in effective porosity is expected since the net-to-gross data is available. A considerable percentage of impermeable shale is present in the cell of some regions in the model.

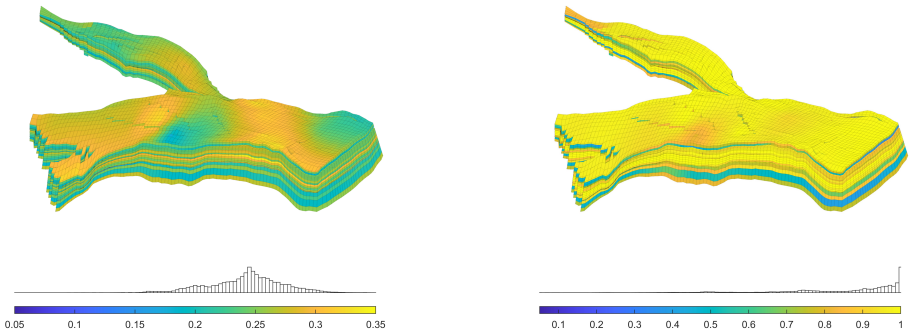

Figure 4.15: Porosity and N/G for the Norne Field. The left graph shows the model's porosity, and the right one shows net-to-gross mapped in the structural model.

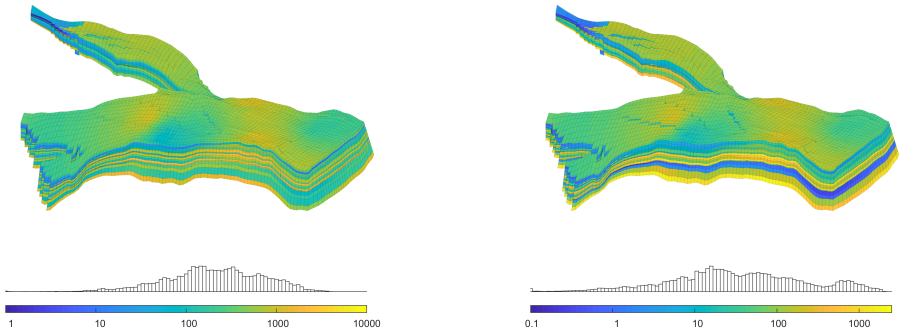

Figure 4.16: Permeability map of the Norne field. The upper-left figure shows the horizontal permeability, and the upper-right figure shows vertical permeability; both are plotted using a logarithmic color scale.

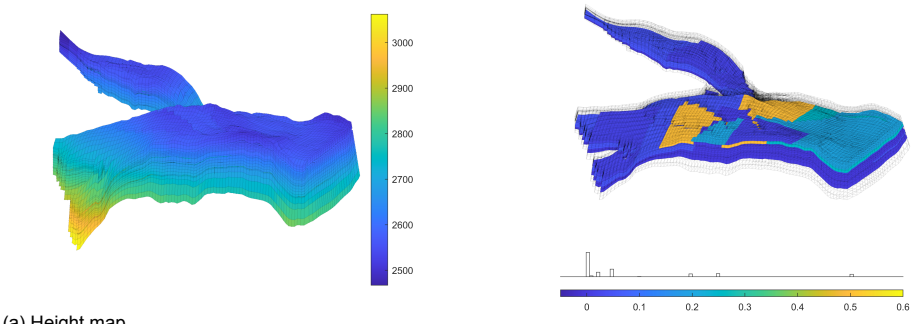

(a) Height map

(b) Transmissibility multipliers

Figure 4.17: Depth map of the Norne field and the vertical multipliers that reduce the vertical communication between grid cells.

5

Simulation Results

A series of numerical results in 3D test cases are presented in this chapter to demonstrate the capabilities of the pEDFM implementation developed in fracture networks modelling overlapped in realistic reservoir models. Six test cases and the results are showed: a Cartesian grid model, a corner point grid model, the SAIGUP model, the Brugge Model, Johansen Formation, and the Norne Field. The geometry and the mesh of the reservoir models were generated using the open-source simulator MRST [33], which allowed processing the input data in ECLIPSE format. Fractures networks were exclusively designed by the author of this work for each model and did not resemble any fracture network. The input parameters' values for fractures and source terms used in the tests are summarized in table 5.1. The models' rock properties were used in the simulations and differed from one model to another one.

5.1. Test Case 1: 3D Homogeneous fractured reservoir (Cartesian Box)

The first case demonstrates the capability of the pEDFM method on Cartesian domains. A 3D domain (100m × 100m × 40m) that contains a lower-dimensional fracture network of 15 elements with different geometrical properties is considered (figure 5.1). The rock matrix is divided on a 50 × 50 × 20 grid, and the fracture network is discretized in 847 grids. A total of 50847 grid cells are considered for the simulation.

The rock matrix has permeability of K_m = 10^{-14} m^2 and rock porosity of ϕ = 0.3. Fracture network contents both highly conductive fractures and flow barriers with permeability of K_f = 10^{-8} m^2 and K_f = 10^{-20} m^2 respectively. Two different scenarios are showed in Test case 1: 5.1(c) represents the scenario 2 that in the opposite version of scenario 1 5.1(b): low conductive fractures are now high conductive fractures and vice versa.

Two injection wells are placed on the bottom left and bottom right corners of the model with a pressure of p_{inj} = 5 × 10^7 Pa. Similarly, two production wells are located at the top left and top right corner (p_{prod} = 1 × 10^7 Pa). The wells are vertical and drilled the whole thickness of the reservoir. Figure 5.2 illustrates the results of the simulation.

Property	**Value**
Fractures permeability (min)	$10^{-20}\ [m^2]$
Fractures permeability (max)	$10^{-8}\ [m^2]$
Fracture aperture	$5 \times 10^{-3}\ [m]$
Initial pressure of the reservoir	$2 \times 10^{7}\ [Pa]$
Injection pressure	$5 \times 10^{7}\ [Pa]$
Production pressure	$1 \times 10^{7}\ [Pa]$

Table 5.1: The identical parameters for all test cases.

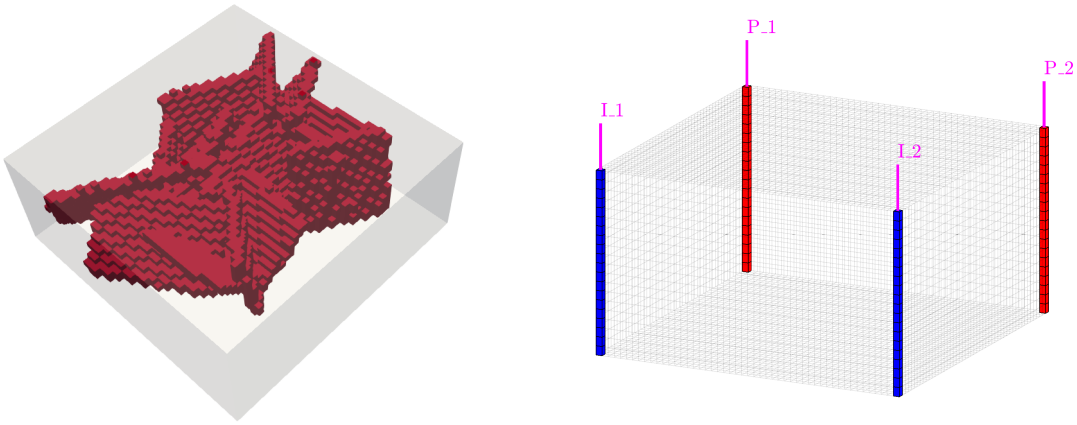

(a) Matrix Cells Fractured

(b) Well Setting

Figure 5.1: Test case 1: A Cartesian model with 15 embedded fractures.

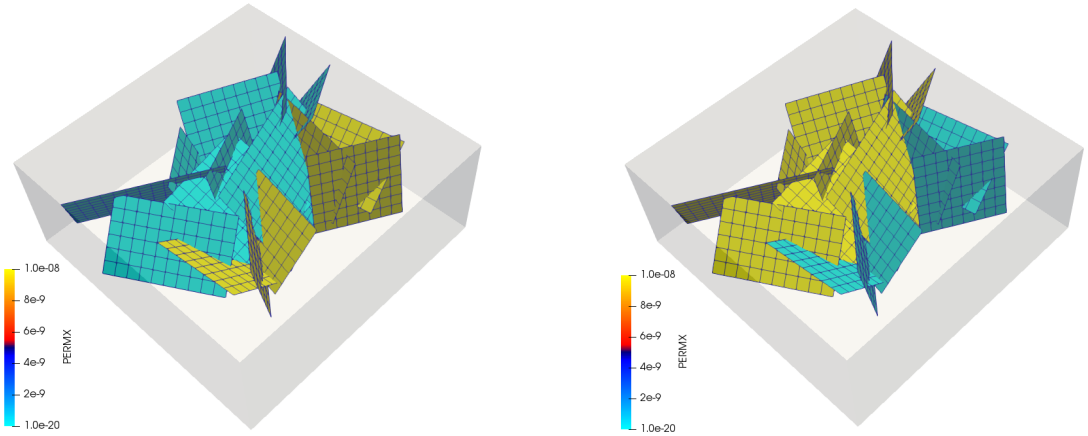

(a) Permeability Fractures: Test Case - Scenario 1

(b) Permeability Fractures: Test Case - Scenario 2

Figure 5.2: Test case 1: A Cartesian model with 15 embedded fractures (scenarios).

The results of the scenario (figure 5.2(a)) are showed in figure 5.3. The flow barriers are near the injection wells, and their effect in the saturation displacement is noticed in the figure 5.3(b). The water influx goes for is restricted to the boundaries of the model. Also, a high-pressure zone figure 5.3(a) is formed near the injection wells as the low permeability fractures limit the flux.

The results of the scenario (figure 5.2(b)) are showed in figure 5.4. The high conductive fractures are near the injection wells, and saturation profile increases through the whole thickness of the reservoir model (figure 5.3(b)). The pressure profiles is uniformly distributed in the the reservoir model figure 5.3(a).

5.2. Test Case 2: 3D Homogeneous fractured reservoir (Corner Point Grid Model)

The second case (figure 5.5) demonstrates the capability of pEDFM method on the reservoir model based on corner point grids. The grid cells in Test case 1 were deformed to create a distorted version of that model. The model does not contain faults but allows us to test the pEDFM implementation in a non-orthogonal grid model. The same dimensions and gridding of test 1 were used in test 2. The fracture network is discretized in 876 grids, and a total of 50876 grid cells are considered for the simulation.

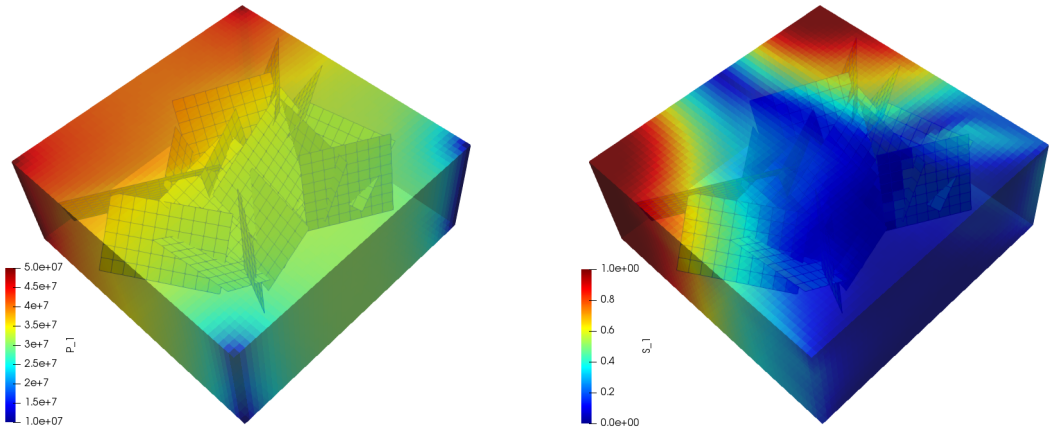

(a) Pressure: Cartesian grid (Scenario 1) (b) Saturation: Cartesian grid (Scenario 1)

Figure 5.3: 3D Homogeneous Cartesian domain: Scenario 1 (Figure 5.2(a)). The figures a and b show the pressure and saturation results on a specific time step.

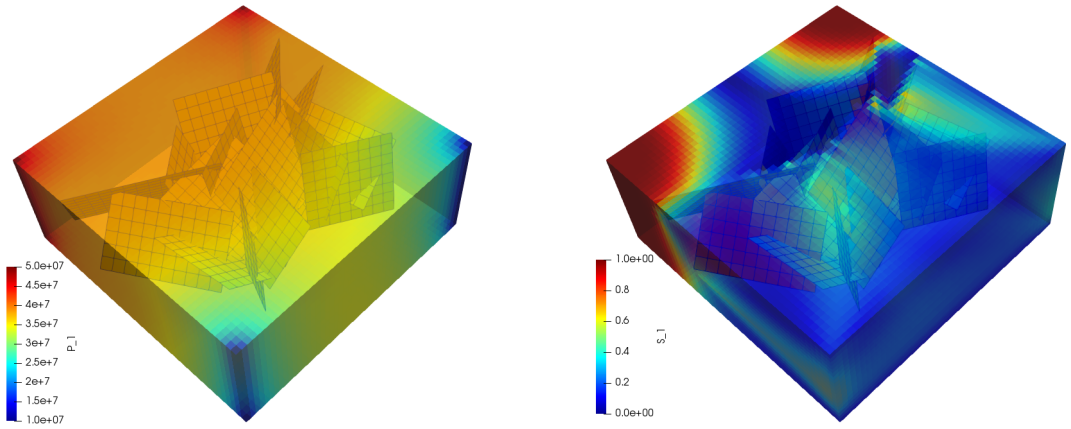

(a) Pressure: Cartesian grid (Scenario 2) (b) Saturation: Cartesian grid (Scenario 2)

Figure 5.4: 3D Homogeneous Cartesian domain: Scenario 2 (Figure 5.2(b)). The figures a and b show the pressure and saturation results on a specific time step.

Similarly to test case 1, two different scenarios are showed in Test case 2: (5.6a) represents the scenario 2 that is the opposite version of scenario 1 (5.6b): low conductive fractures are now high conductive fractures and vice versa. Values of permeability for matrix and fractures are the same as in test 1. The well pattern and pressure restrictions are the same as in the previous case.

The results of the scenario (figure 5.6(a)) are showed in figure 5.7. It is not possible to compare Test Case 1 since the grid cells are not orthogonal in Test Case 2, which implies another type of cell geometry. The same fracture network for Test Case 1 was used in Case 2, and a similar pressure and saturation profile is observed in the results.

The flow barriers are close to the injection wells, and they restrict the saturation displacement in the center of the model (figure 5.3(b)). A high-pressure area figure 5.3(a) is created near the injection wells as the low permeability fractures limit the flux through the reservoir model.

The results of the scenario (figure 5.6(b)) are showed in figure 5.8. The high conductive fractures are near the injection wells, and the saturation profile increases through the whole thickness of the reservoir model (figure 5.7(b)). The saturation profile resembles the obtained in Test Case 1. The pressure profile is uniformly distributed in the reservoir model figure 5.7(a) as there is no flux restriction near the wells.

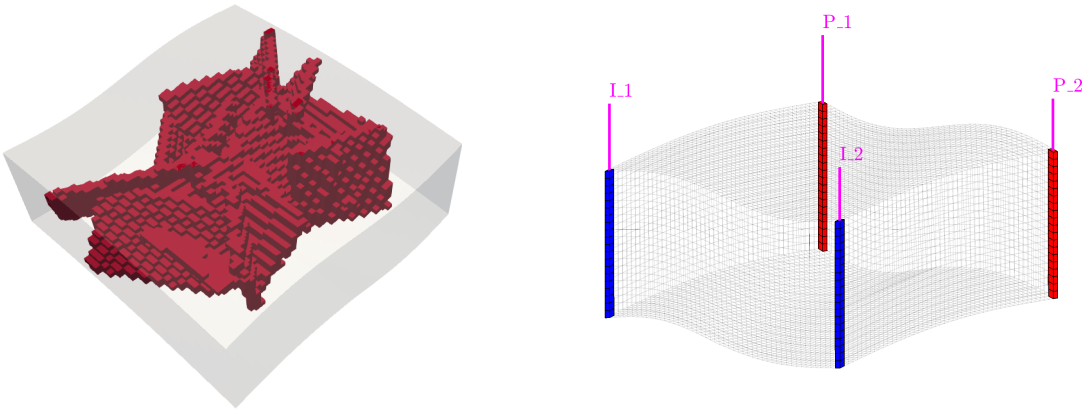

(a) Matrix Cells Fractured

(b) Well Setting

Figure 5.5: Test case 1: A corner point grid model with 15 embedded fractures.

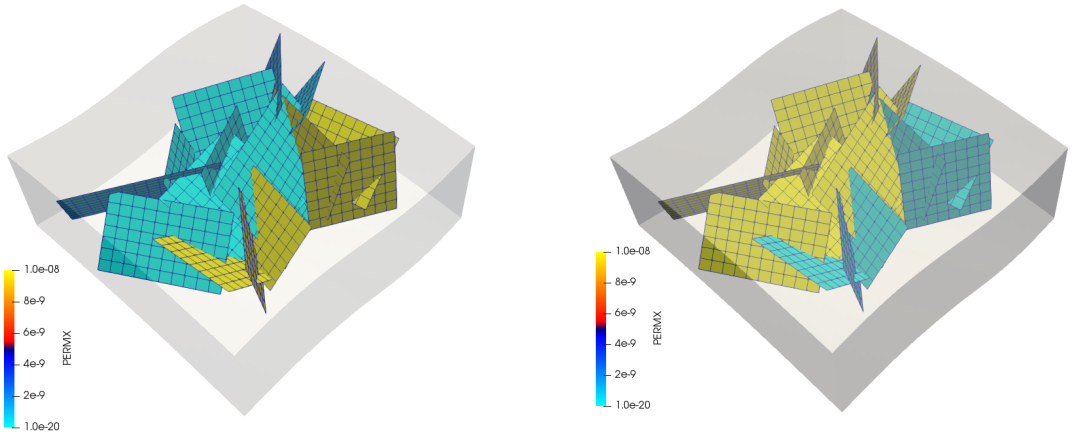

(a) Permeability Fractures: Scenario 1

(b) Permeability Fractures: Scenario 2

Figure 5.6: Test case 1: A corner point grid model with 15 embedded fractures (scenarios).

5.3. Test Case 3: SAIGUP Model

The following test case shows fracture modeling results with pEDFM in a synthetic geologically relevant corner-point grid model. The reservoir model consists of 40 x 120 x 20 grid cells from which 78720 grid cells are active. The available realization of rock properties was used in the simulation. A network of 53 fractures is embedded in the reservoir domain that contents both highly conductive fractures and flow barriers with permeability of K_f = 10^{-8} m^2 and K_f = 10^{-20} m^2 respectively. The fracture network consists of 3163 grid cells (in total, 81883 grid cells). Four injection wells with a p_{inj} = 5 × 10^7 Pa and three production wells with a p_{prod} = 1 × 10^7 Pa were defined in the model. Wells are drilled vertical and through the entire thickness of the reservoir.

The results of the simulation are showed in figures 5.11 and 5.12. The production wells are surrounded by low conductivity fractures that have difficulty in the flow through them. The pressure results are shown in figure 5.11. The pressure is considerably distributed in the reservoir except in the production wells area. The saturation results at three different time steps are shown in figure 5.12. The water saturation has increased in the conductive fractured cells since they improve the flow through the reservoir's fractured areas.

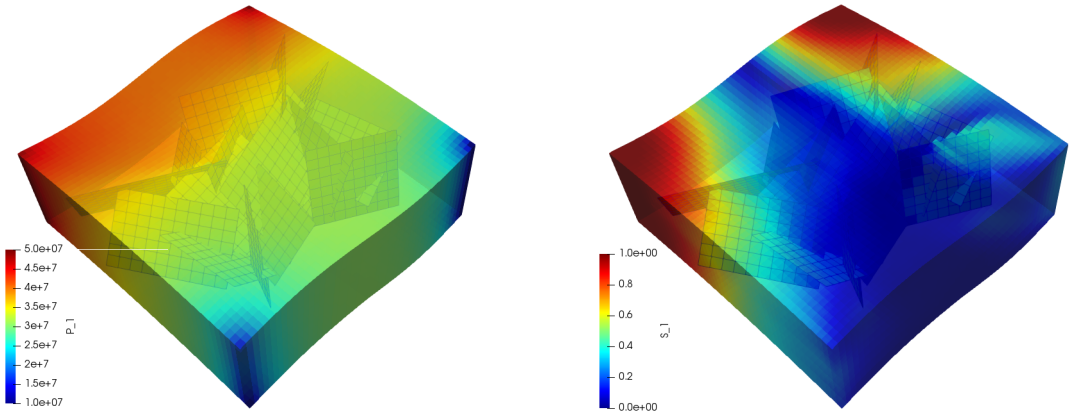

(a) Pressure: Cartesian grid (Scenario 1) (b) Saturation: Cartesian grid (Scenario 1)

Figure 5.7: 3D Homogeneous Cartesian domain: Scenario 1 (Figure 5.6(a)). The figures a and b show the pressure and saturation results on a specific time step.

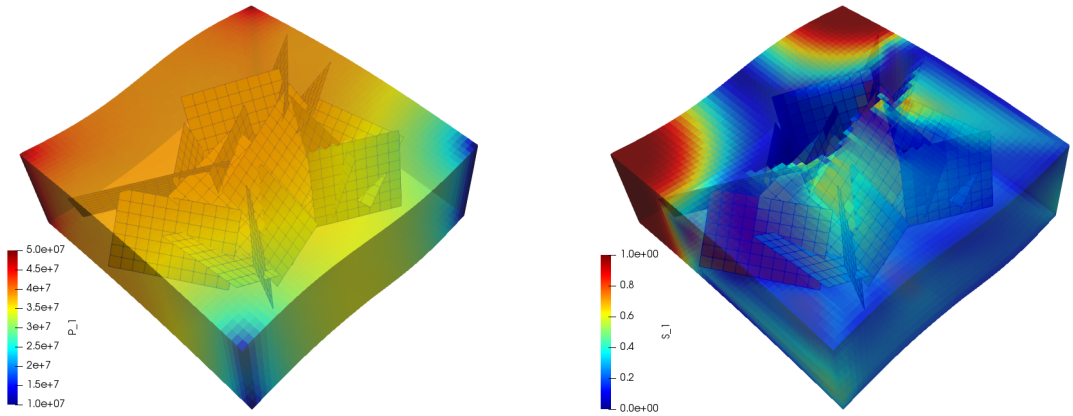

(a) Pressure: Cartesian grid (Scenario 2) (b) Saturation: Cartesian grid (Scenario 2)

Figure 5.8: 3D Homogeneous Cartesian domain: Scenario 2 (Figure 5.6(b)). The figures a and b show the pressure and saturation results on a specific time step.

5.4. Test Case 4: Brugge Model

The following test case shows the pEDFM model's capability on fracture modeling in a synthetic geologically relevant corner-point grid model. The reservoir model consists of 138 x 48 x 9 grid cells from which 43474 grid cells are active. Rock properties of the realization available on public data were used in the simulation. A network of 60 fractures is embedded in the reservoir domain that contents both highly conductive fractures and flow barriers with permeability of K_f = 10^{-8} m^2 and K_f = 10^{-20} m^2 respectively. The fracture network consists of 5384 grid cells (in total 48858 grid cells). The well pattern settle was a modified version of the original well pattern (20 wells) [44]. Four injection wells with a p_{inj} = 5 × 10^7 Pa and three production wells with a p_{prod} = 1 × 10^7 Pa were defined in the model. Wells are drilled vertical and through the entire thickness of the reservoir.

The results of the scenario (figure 5.14(a)) are showed in figures 5.15 and 5.16. The injection wells are surrounded by high conductivity fractures that facilitate the flow in the reservoir model. The pressure is considerably distributed in the whole reservoir, as it can see it in figure 5.15(a). The saturation displacement is considerable enhanced with the high conductive fractures (figure 5.15(a)). The water saturation is increased in the fractures cells since they improve the flow through the reservoir's fractured areas.

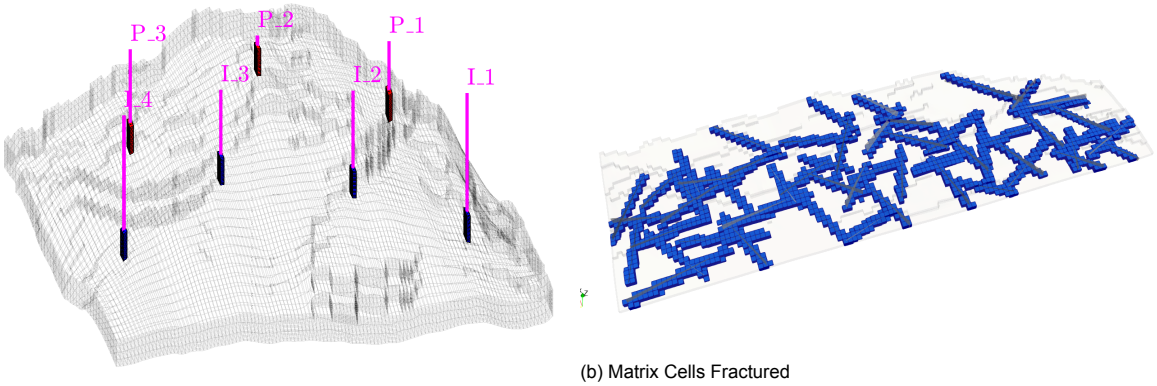

(a) Well Pattern

(b) Matrix Cells Fractured

Figure 5.9: Test case 3: SAIGUP Model with a set of 53 fractures.

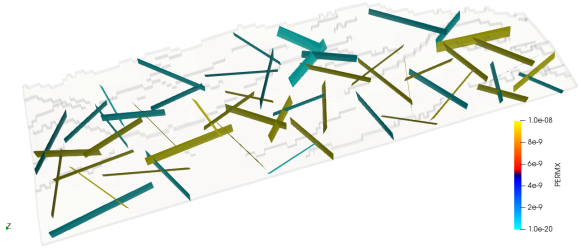

Figure 5.10: Test case 3: SAIGUP Model (Permeability Fractures).

The results of the scenario (figure 5.14(b)) are showed in figures 5.17 and 5.18. The injection wells are surrounded by flow barriers that restrict the flow. As a result of them, a high-pressure zone is formed near the wells since the central area of the reservoir is isolated with low permeability fractures (figure 5.17(a)). The saturation displacement is small since the reservoir's low permeability values and the no existence of high conductive fractures improved the model's permeability. The saturation displacement is restricted to the area near the injection well (figure 5.18).

5.5. Test Case 5: The Johansen Formation

The "NPD5" sector of the Johansen formation model [33] is used in the following test case. It is a corner-point grid reservoir model that consists of 100 x 100 x 11 grid cells from which 88775 grid cells are active. The rock properties of the Johansen formation available on public data were as input in the simulation. A network of 121 fractures is embedded in the reservoir domain that contents both highly conductive fractures and flow barriers with permeability of K_f = 10^{-8} m^2 and K_f = 10^{-20} m^2 respectively. The model is bounded for two shale formations, so the fractures were placed inside the Johansen formation (layers 6 to 10). 150 fractures are embedded in the model, and the fracture network consists of 3494 grid cells (in total 92269 cells). Five injection wells with a p_{inj} = 5 × 10^7 Pa and four production wells with a p_{prod} = 1 × 10^7 Pa were placed in the model. Wells are vertical and drilled through the entire thickness of the model.

The results of the simulation of a fracture network in the Johansen formation (scenario 1 (5.20a) are showed in figures 5.21 and 5.22.

The injection wells are surrounded by high conductivity fractures that facilitate a reservoir model flow since the model's dimensions are considerably big (approximately 50 km x 50 km). The pressure is distributed substantially in the whole reservoir, as shown in figure 5.21(a). High pressure in the entire reservoir is observed since there is no restriction for flowing and two shale formations bound the Johansen sandstone. In low-pressure areas, it is possible to interpret that low permeable fractures

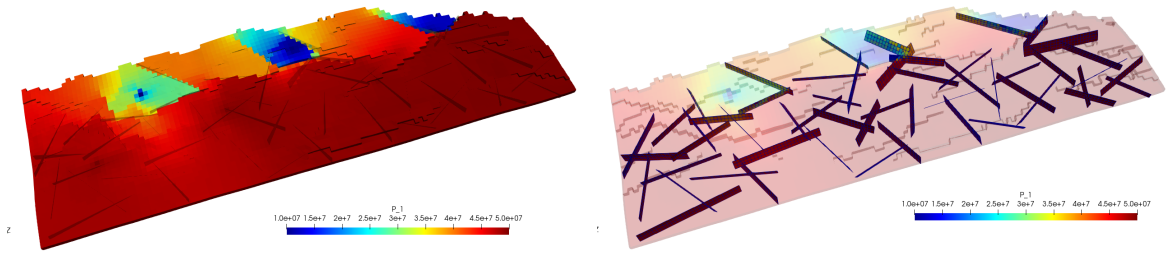

Figure 5.11: pEDFM simulation results of pressure in the SAIGUP Model. The left figure shows the reservoir model results, and the right one highlights the result in the fracture network. Results are at simulation time 5000 [days].

border these areas. The saturation displacement is considerable enhanced with the high conductive fractures (figure 5.22) located near to the injector wells. Based on the results, they can improve the model's conductivity since there is an increase in saturation in the area near the injector wells.

The results of the simulation of a fracture network in the Johansen formation (scenario 2 (5.20b) are showed in figures 5.23 and 5.24.

The injection wells are surrounded by low conductivity fractures that restrict the reservoir model. The pressure distribution differs considerably with respect to scenario 1. The wells' flow barriers avoid the high pressure of the injectors well being distributed in the whole formation. The saturation displacement (figure 5.24) is less than scenario one since the low conductive fractures are located near the injector wells.

5.6. Test Case 6: The Norne Field

The reservoir model of the Norne field model consists of 46 x 122 x 22 grid blocks. The corner-point grid reservoir model has 44915 active grid cells. The rock properties of the Norne field available on public data were used in the simulation. A set of 56 fractures is embedded in the reservoir domain and comprises highly conductive fractures and flow barriers with permeability of K_f = 10^{-8} m^2 and K_f = 10^{-20} m^2respectively. Fifty-six fractures are embedded in the model, and the fracture network consists of 2165 grid cells (in total, 48705 cells). Four injection wells with a p_{inj} = 5 × 10^7 Pa and three production wells with a p_{prod} = 1 × 10^7 Pa were placed in the model. Wells are vertical and drilled through the entire thickness of the model.

The results of the scenario (figure 5.26(a)) are showed in figures 5.27 and 5.28. The injection wells are surrounded by flow barriers that restrict the saturation displacement in the reservoir. The pressure is considerably high in the areas near the wells. These high-pressure areas are an indication that the pEDFM implementation is successful in the modeling of the fractures with low conductivity. In the nearby area of two injectors wells the fractures were placed to recreate a flow pattern. In figure 5.28 shows that the increase in saturation is mainly carried out in two areas. These two areas are not isolated from the model and allow distribution in the new saturation through these flow paths.

The results of the scenario (figure 5.26(b)) are showed in figures 5.29 and 5.30. The injection wells are surrounded by high conductivity fractures that facilitate a reservoir model. The pressure is more uniformly distributed (figure 5.29(a)) concerning the previous cause as it results in the improved conductivity of the area nearby to the injector wells. It is possible to realize where are located flow barriers since the ”fingers” of the reservoir model has considerably lower pressure values. Similarly, the effect of high permeable fracture near the injector wells has boosted the saturation displacement, as shown in figure 5.30. The water saturation is increased in the fractures cells since they improve the flow through the reservoir's fractured areas.

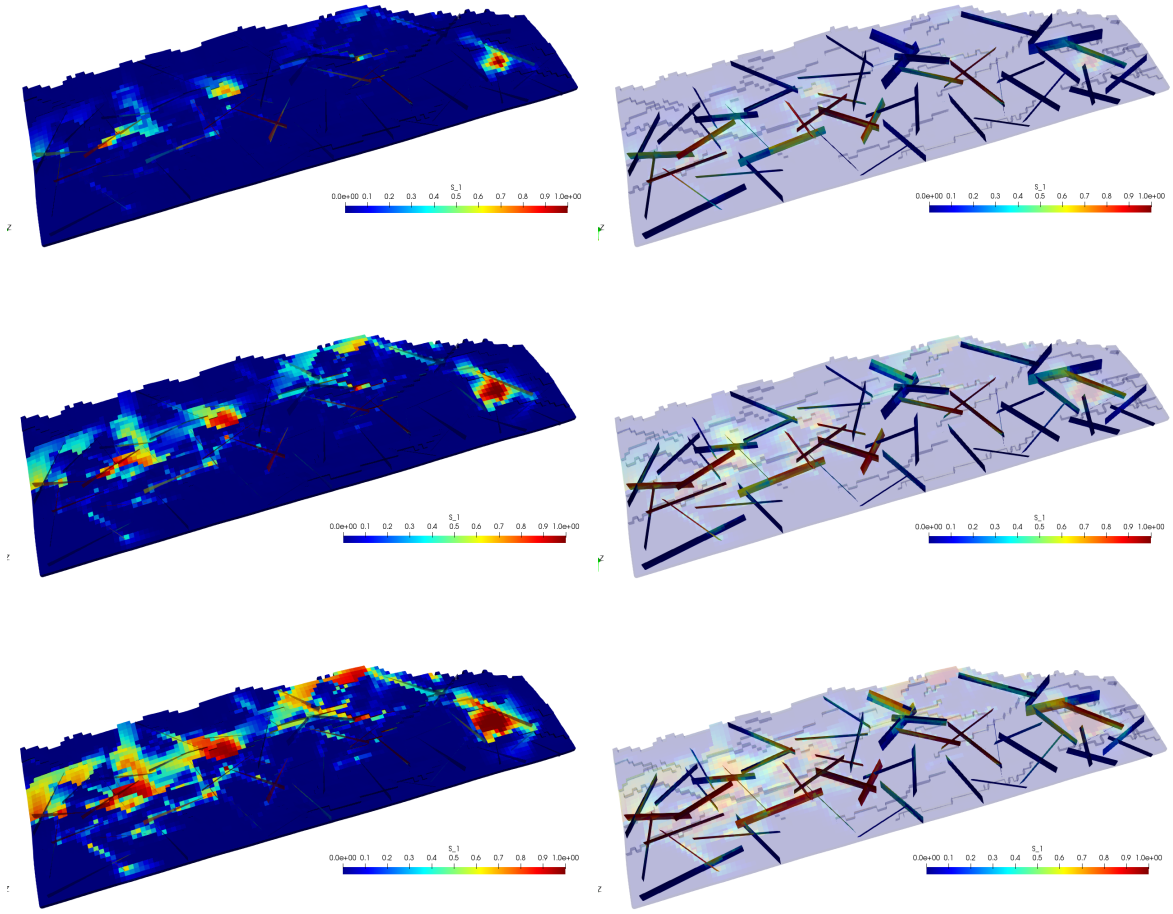

Figure 5.12: pEDFM simulation results of saturation in the SAIGUP Model. The first column shows the results in the reservoir model. The second column shows the result in the fracture network. Row wise, the simulation time increases from 2000 to 5000 to 10000 [days].

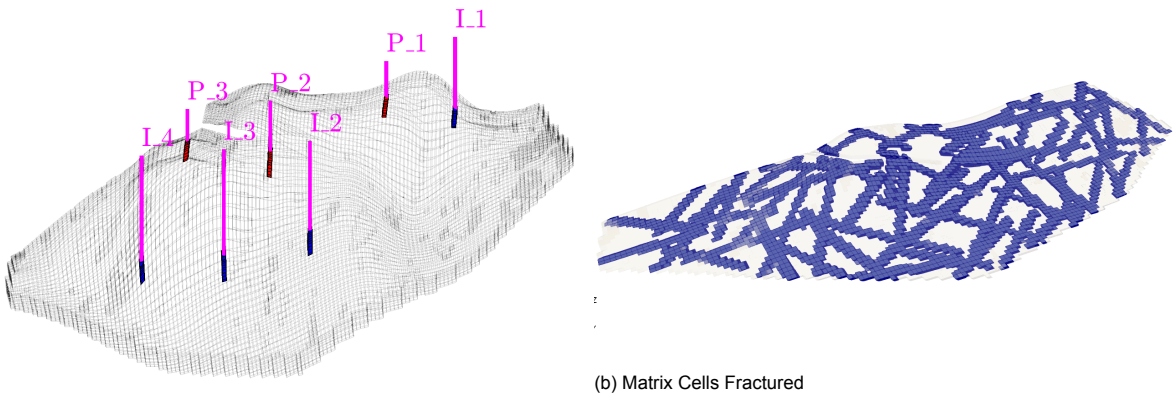

(a) Well Pattern

(b) Matrix Cells Fractured

Figure 5.13: Test case 4: Brugge Model with a set of 60 fractures.

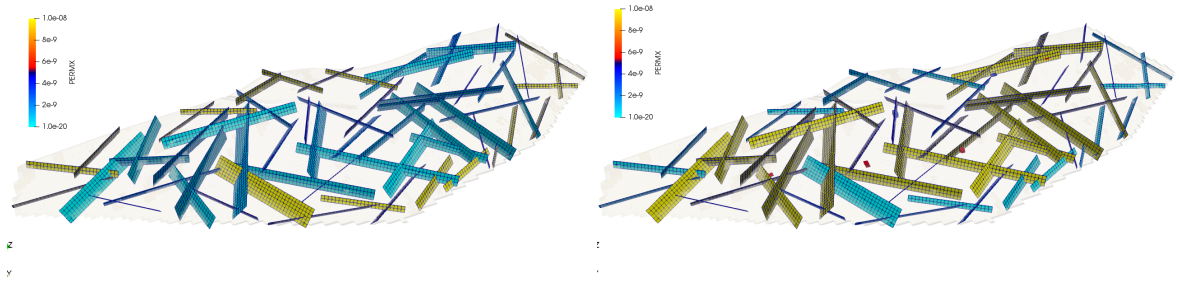

(a) Scenario 1 (b) Scenario 2

Figure 5.14: Test case 4: Brugge Model with a set of 60 fractures (scenarios).

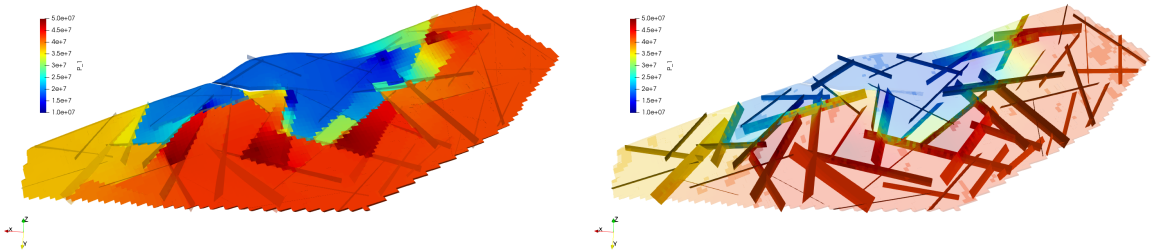

Figure 5.15: pEDFM simulation results of saturation for the Brugge Model (scenario 1 (5.14a). The left figure shows the reservoir model results, and the right one highlights the result in the fracture network. Results are at simulation time 5000 [days].

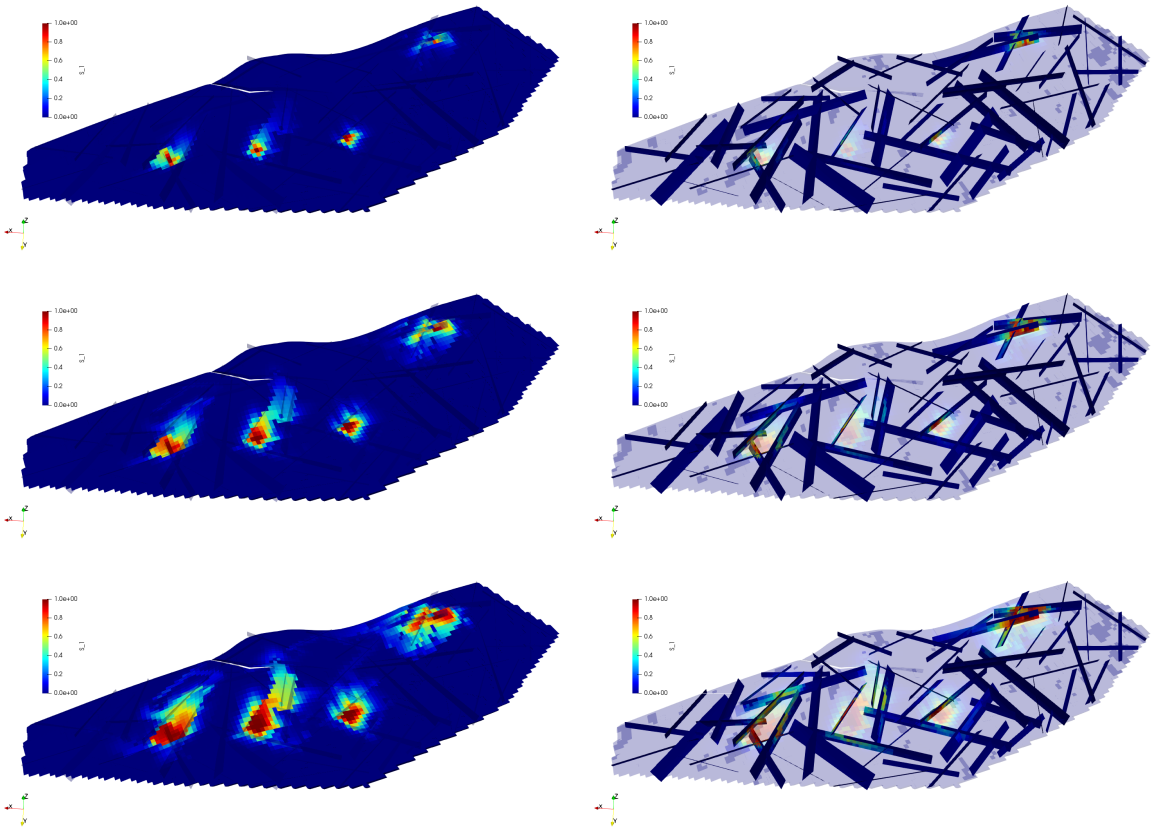

Figure 5.16: pEDFM simulation results of saturation in the Brugge Model (Scenario 1 (5.14a). The first column shows the results in the reservoir model. The second column shows the result in the fracture network. Row wise, the simulation time increases from 2000 to 5000 to 10000 [days].

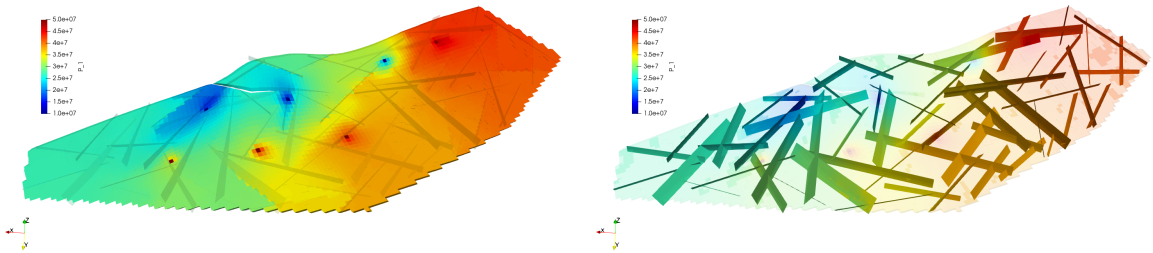

Figure 5.17: pEDFM simulation results of saturation for the Brugge Model (scenario 2 (5.14b). The left figure shows the reservoir model results, and the right one highlights the result in the fracture network. Results are at simulation time 5000 [days].

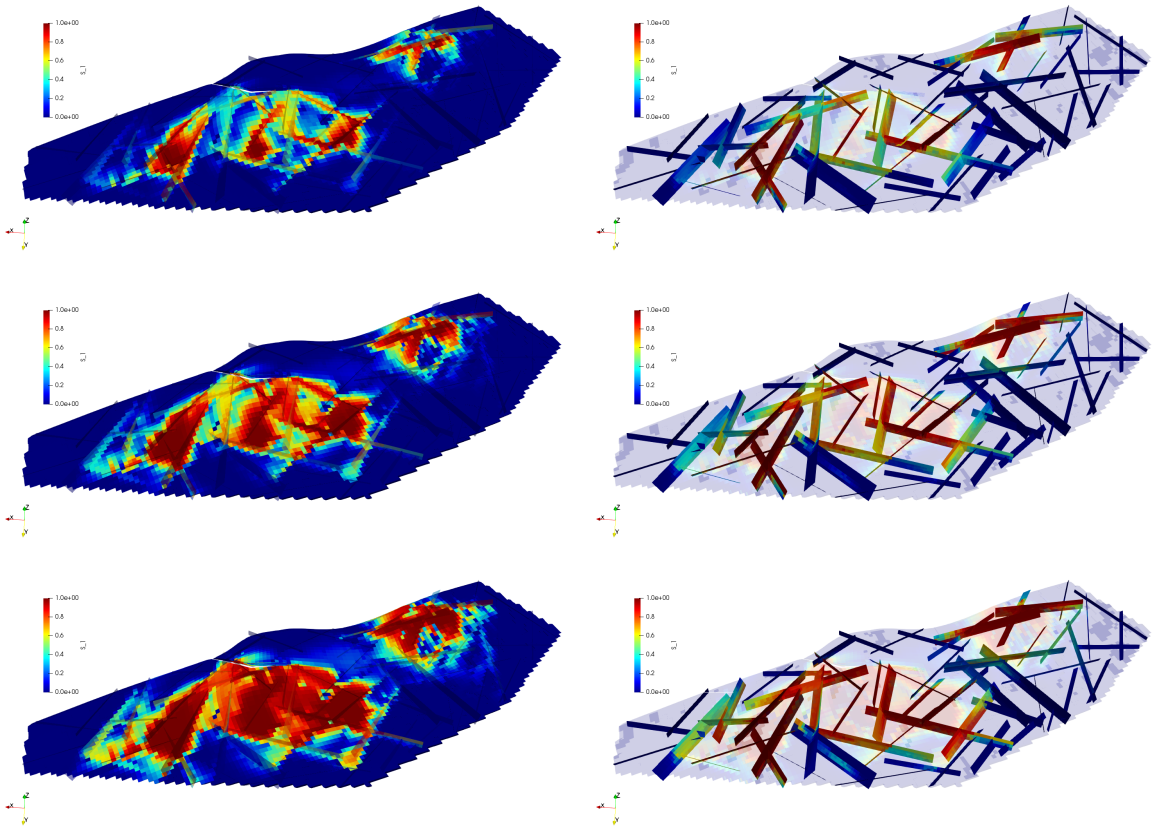

Figure 5.18: pEDFM simulation results of saturation in the Brugge Model (scenario 2 (5.14b). The first column shows the results in the reservoir model. The second column shows the result in the fracture network. Row wise, the simulation time increases from 2000 to 5000 to 10000 [days].

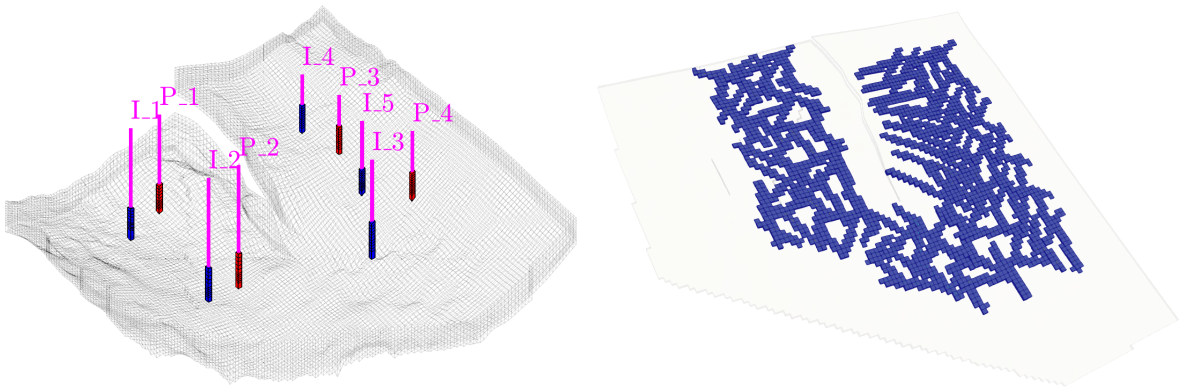

(a) Well Pattern

(b) Matrix Cells Fractured

Figure 5.19: Test case 4: The Johansen Formation with a set of 121 fractures.

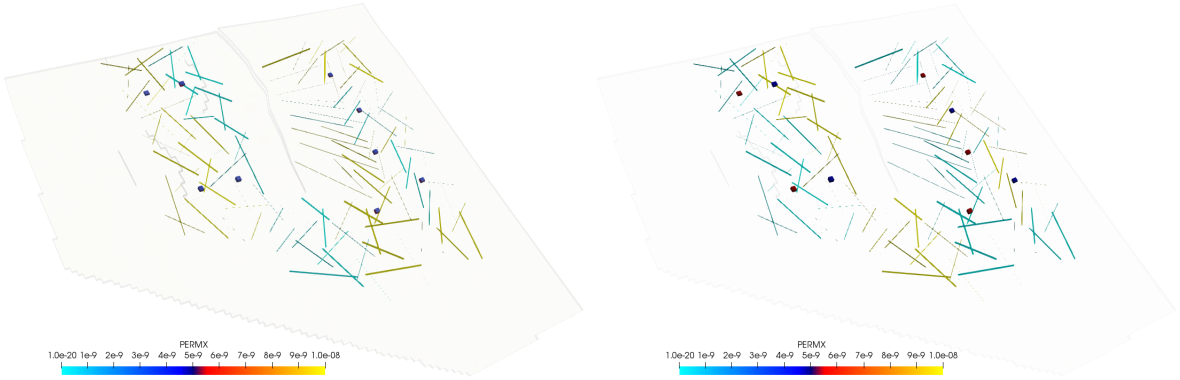

(a) Scenario 1

(b) Scenario 2

Figure 5.20: Test case 4: The Johansen Formation with a set of 121 fractures (scenarios).

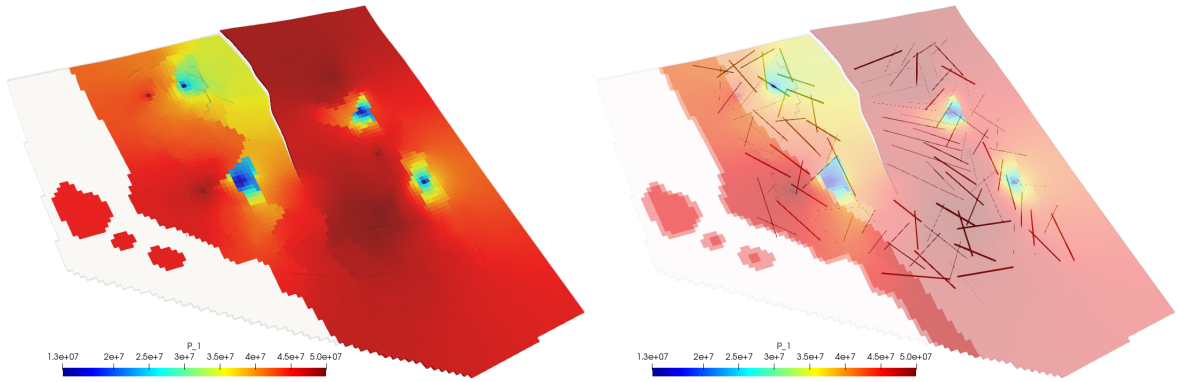

(a) Pressure: Matrix

(b) Pressure: Fractures

Figure 5.21: pEDFM simulation results of pressure in the Johansen Formation (scenario 1 (5.20a). The left figure shows the reservoir model results, and the right one highlights the result in the fracture network. Results are at simulation time 20000 [days].

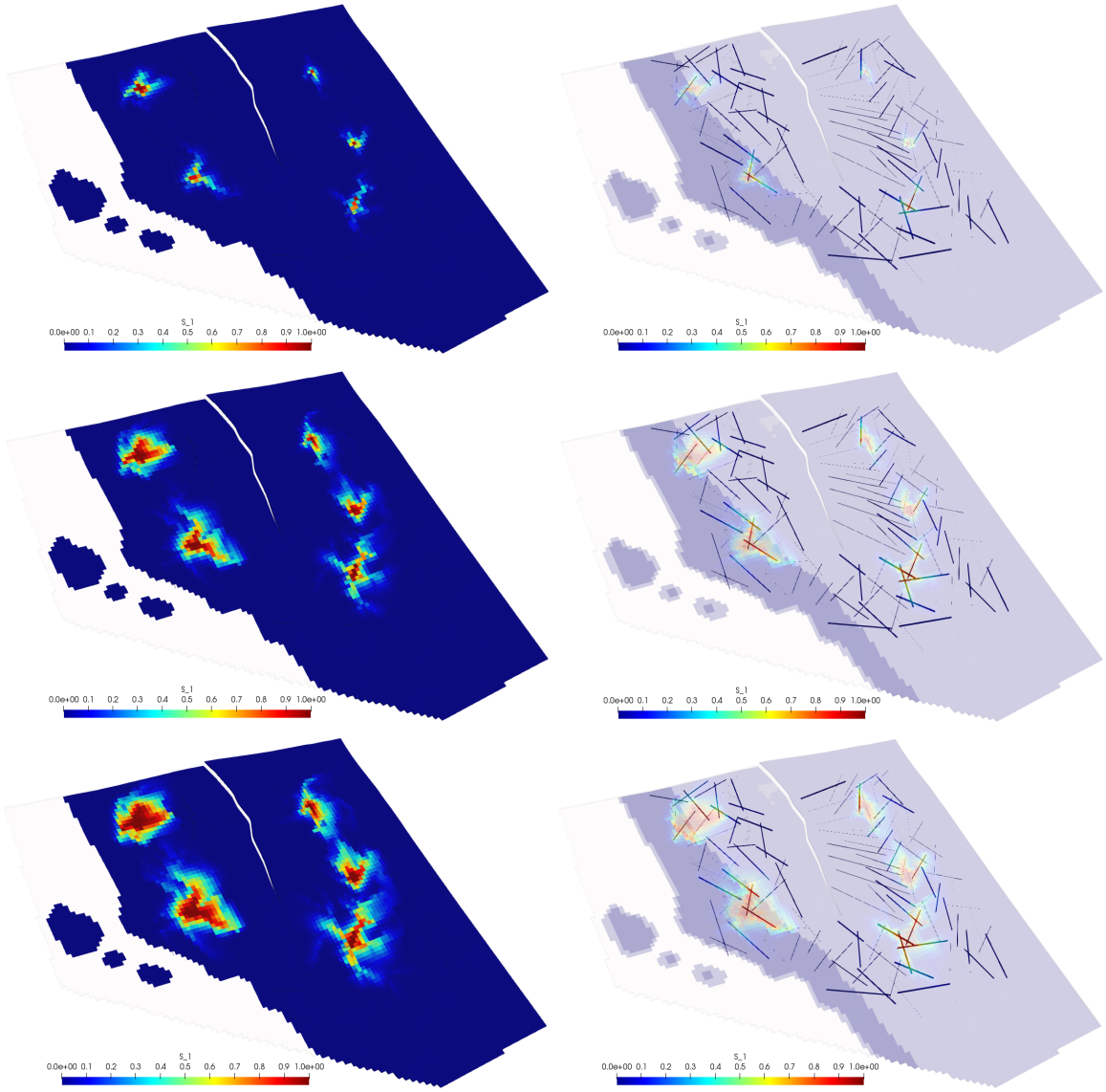

Figure 5.22: pEDFM simulation results of saturation for the Johansen Formation (scenario 1 (5.20a). The first column shows the results in the reservoir model. The second column shows the result in the fracture network. Row wise, the simulation time increases from 5000 to 20000 to 35000 [days].

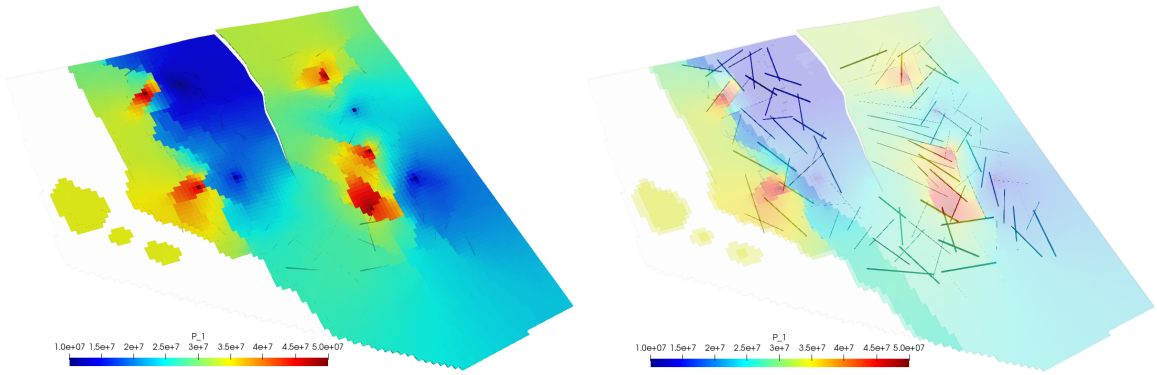

(a) Pressure: Matrix

(b) Pressure: Fractures

Figure 5.23: pEDFM simulation results of pressure in the Johansen Formation (scenario 2 (5.20b). The left figure shows the reservoir model results, and the right one highlights the result in the fracture network. Results are at simulation time 20000 [days].

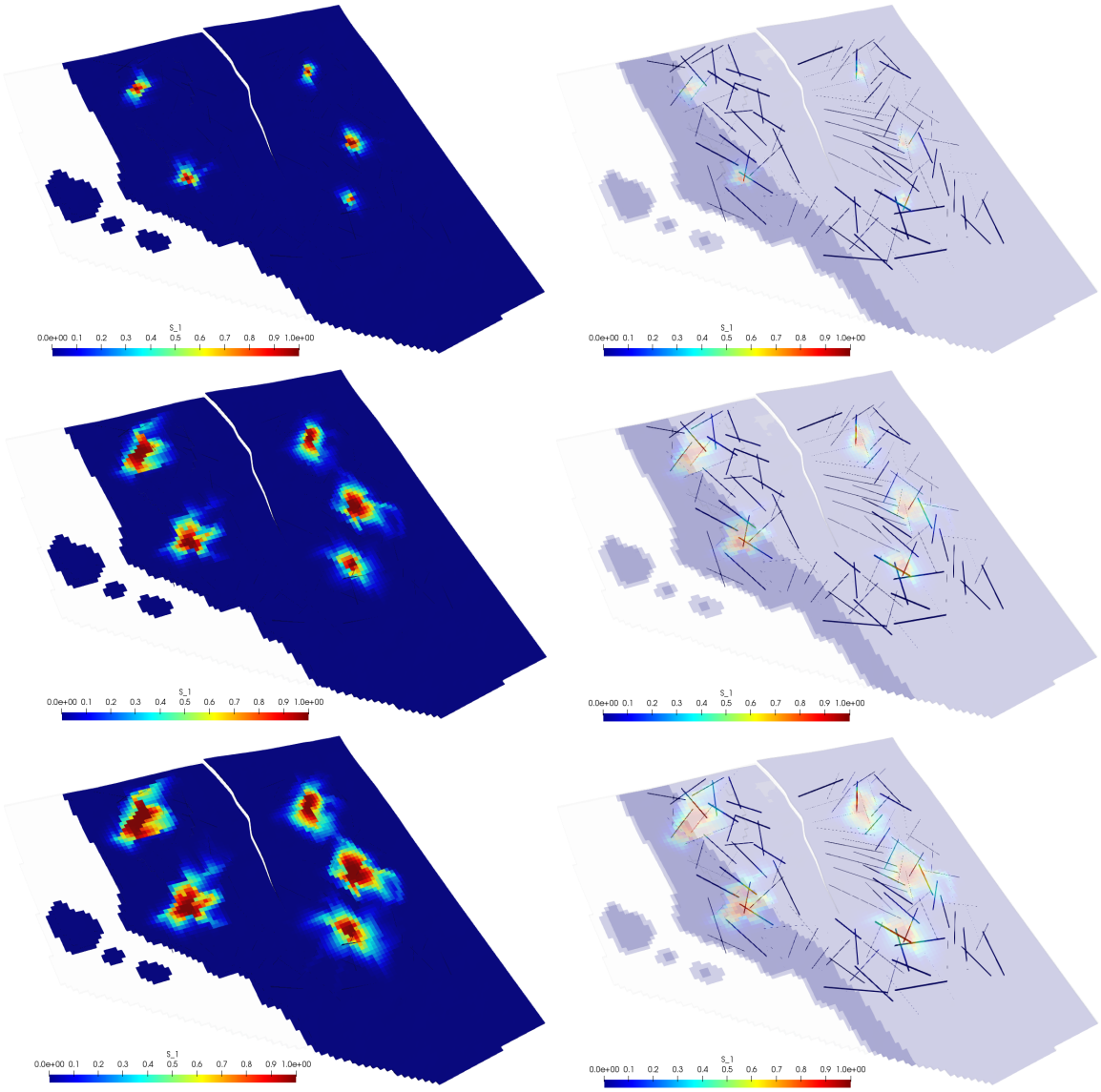

Figure 5.24: pEDFM simulation results of saturation for the Johansen Formation (scenario 2 (5.20b). The first column shows the results in the reservoir model. The second column shows the result in the fracture network. Row wise, the simulation time increases from 5000 to 20000 to 35000 [days].

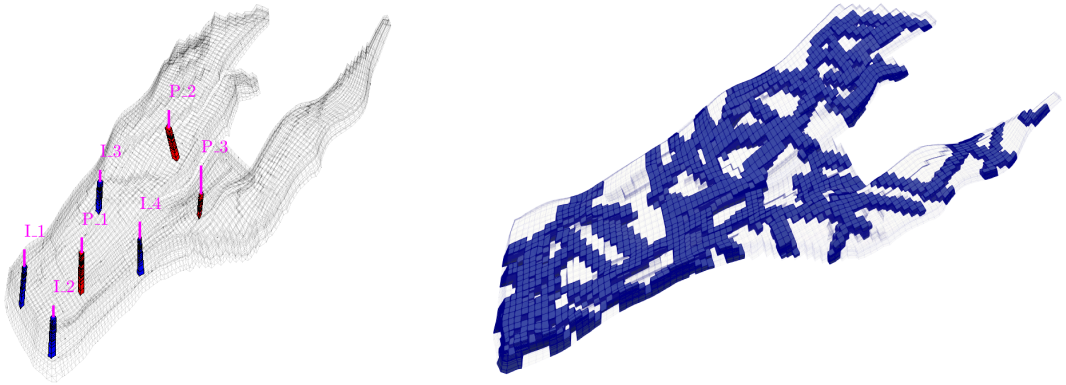

(a) Fractures Permeability

(b) Fractures Cells

Figure 5.25: Test case 5: Norne Field with a set of 56 fractures.

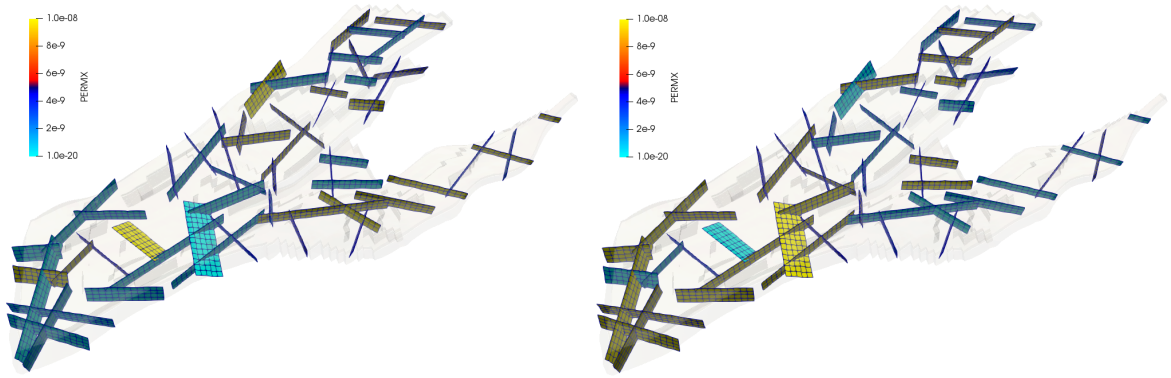

(a) Scenario 1 (b) Scenario 2

Figure 5.26: Test case 4: Norne Field with a set of 56 fractures (scenarios).

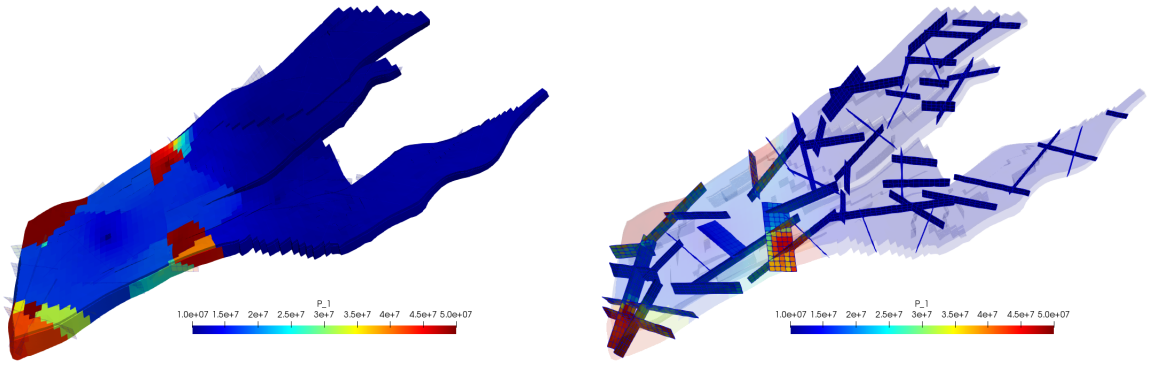

Figure 5.27: pEDFM simulation results of saturation for the Norne Field (scenario 1 (5.26a). The left figure shows the reservoir model results, and the right one highlights the result in the fracture network. Results are at simulation time 5000 [days].

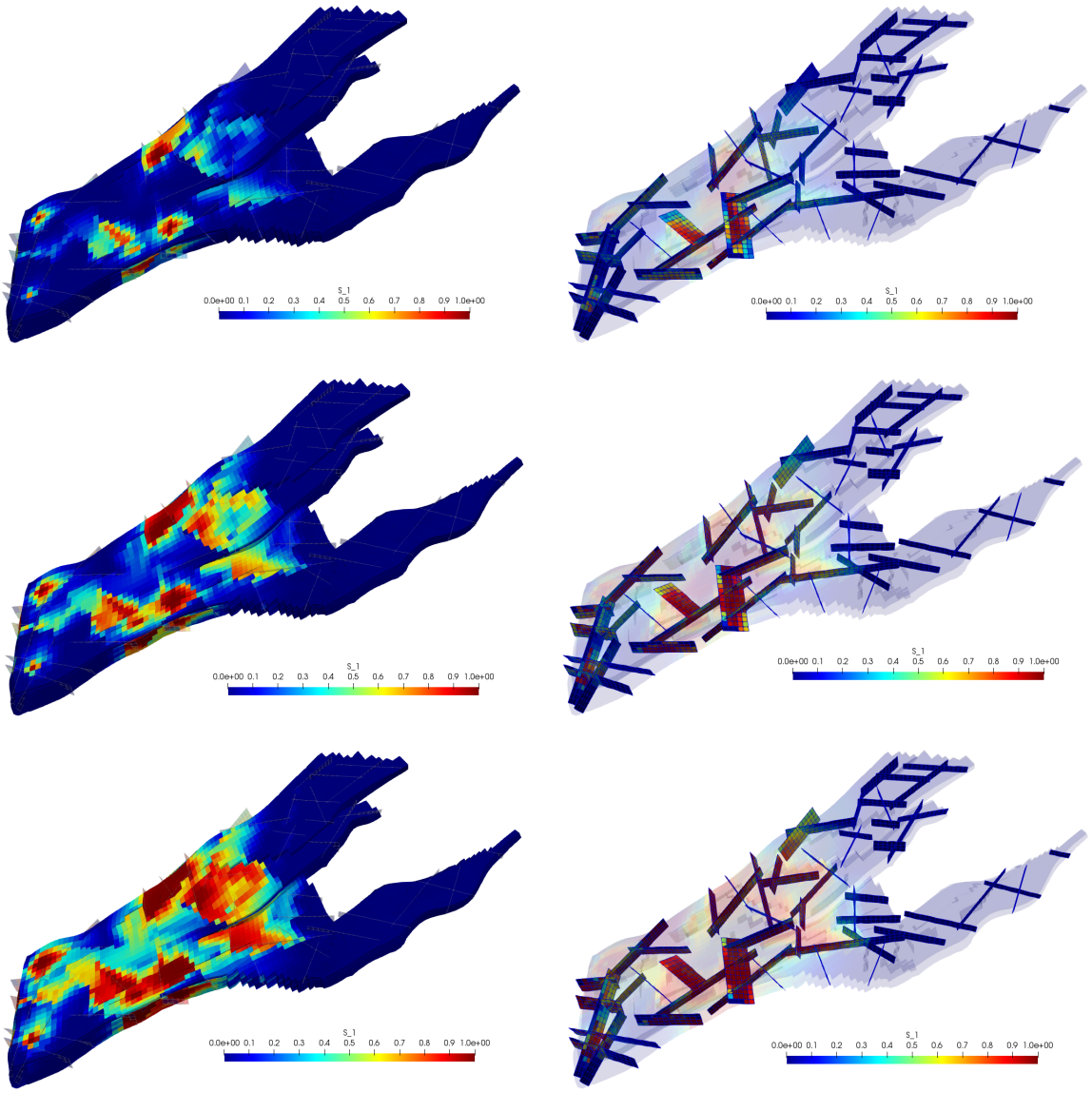

Figure 5.28: pEDFM simulation results of saturation for the Norne Field (scenario 1 (5.26a). The first column shows the results in the reservoir model. The second column shows the result in the fracture network. Row wise, the simulation time increases from 2000 to 5000 to 10000 [days].

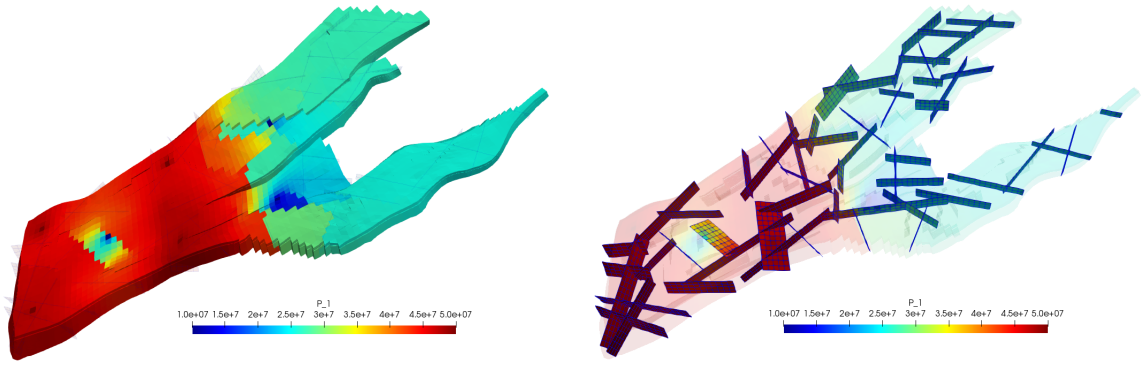

Figure 5.29: pEDFM simulation results of saturation for the Norne Field (scenario 2 (5.26b). The left figure shows the reservoir model results, and the right one highlights the result in the fracture network. Results are at simulation time 5000 [days].

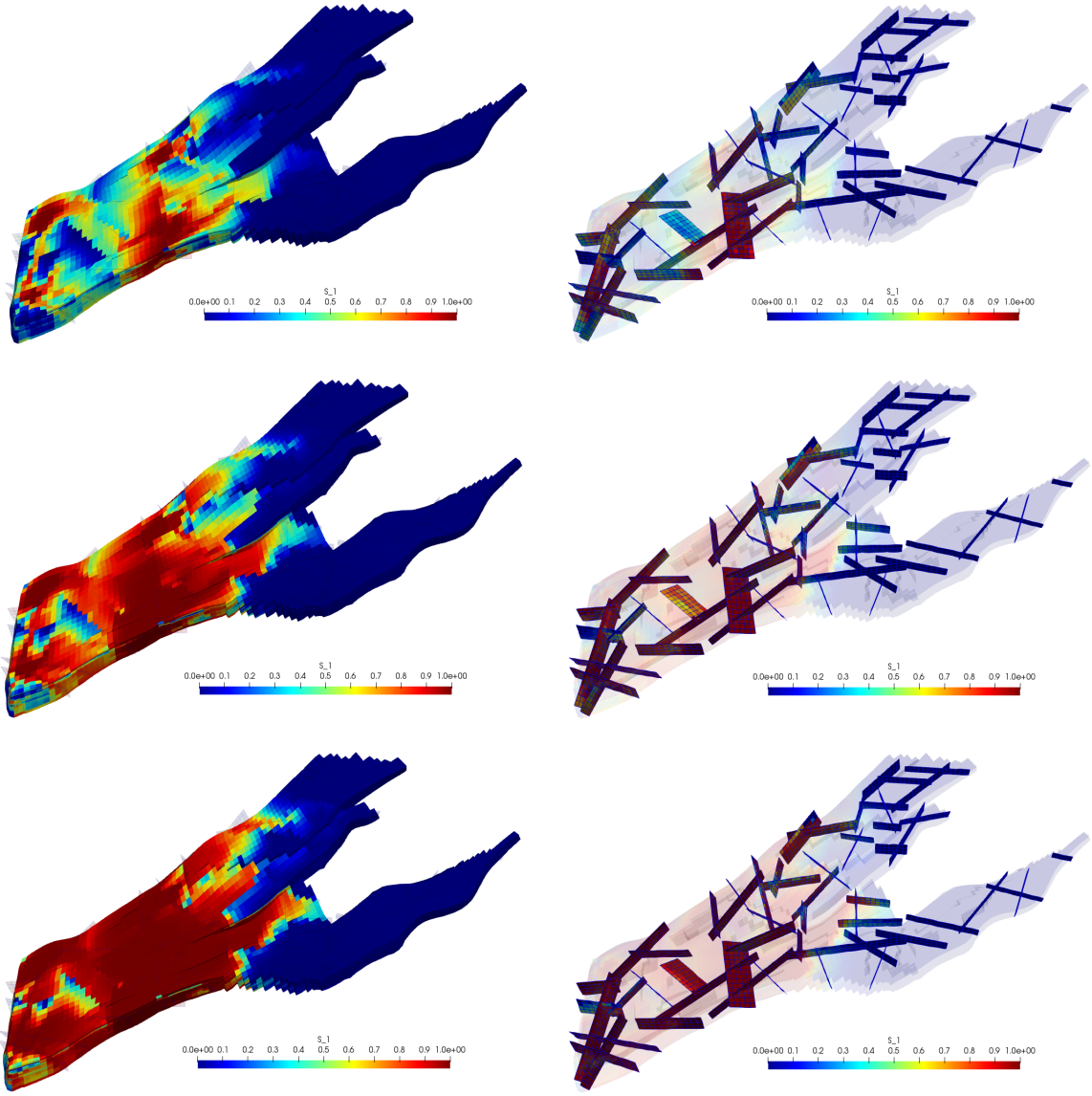

Figure 5.30: pEDFM simulation results of saturation for the Norne Field (scenario 2 (5.26b). The first column shows the results in the reservoir model. The second column shows the result in the fracture network. Row wise, the simulation time increases from 2000 to 5000 to 10000 [days].

6

Conclusions

An implementation of the novel projection-based embedded discrete fracture model (pEDFM) for fracture modeling in reservoir models based on corner-point grid geometry was developed for fully implicit simulation of two-phase flow in fractured heterogeneous porous media. The previous research of the pEDFM model was extended to incorporate and model fracture geometries on a discrete system based on standard corner-point grids. pEDFM is based on the establishment of additional fracture – matrix flux connections.

The developed pEDFM implementation was assessed in a couple of homogeneous reservoirs models and tested in several realistic reservoir models to demonstrate that the application can also consider these models' inherent complex grid cell geometry. The fine-scale simulation in 3D real reservoirs models showed that it was possible to model both highly conductive and flow-barrier fractures in these scenarios with complex geometries and highly heterogeneous rock properties. The simulations results demonstrated that pEDFM is a flexible fracture model that can be extended from cartesian domains to sophisticated reservoir geometries and can still precisely describe the physical impact on the flow patterns in both highly conductive fractures and flow barriers.

Based on the simulation results, it was shown that fracture networks could generate flow paths in the reservoir, hence the importance of modeling these systems. pEDFM could precisely model them and provide simulation results that capture the influence of these flow networks.

6.1. Future Work

The developed pEDFM implementation showed good results in the real test case scenarios. In this section, some topics for further improvements in the pEDFM approach are suggested:

6.1.1. Unstructured Grids

Several features are not possible to easily model with corner point grids, like multiple fault intersections. Unstructured grids can be adapted to complex reservoir structures and domains, and in terms of increasing local resolution, they do not show inconvenient with refinement. An extension of pEDFM to unstructured grids can be considered to prove that the concepts work for different types of grids.

6.1.2. Compositional Simulations

This thesis's results showed that pEDFM could be applied in a reservoir with complex geometries for two-phase immiscible flow. It should be considered simulating multiphase flow simulation with the test cases of this work.

6.1.3. Discretizations for general polyhedral grids

The adjustable cell geometry of the corner point format brings numerous difficulties for numerical implementations. Cell geometries will frequently deviate significantly from being orthogonal, and they introduce unphysical preferred flow path directions in the numerical methods. The TPFA method is only convergent for K-orthogonal grids and consistent for specific combinations of grids and permeability tensors. Corner points grids can be significantly distorted to adapt to the geological features

and results in not K-orthogonal grid cells. Grid orientation effects can be generated due to lack of consistency in the TPFA, not K-orthogonal grid cells.It should be taken in consideration another type of discretization that can allow fixing the inconvenience related to non-orthogonal grids.

A

Multiscale Finite Volume (MSFV) on corner point grids

Reservoir characterization can provide detailed information about the geological structure of commercial interest. Still, simulations become impracticable in high-resolution geological models with the standard models of flow simulation in porous media. Scale transferring methods allows the combination of high-resolution reservoir data in the flow simulation grid. They can be divided into two different approaches: upscaling methods and multiscale methods.

Upscaling methods [13] through homogenization techniques provide effective parameters in a coarse-scale version of the original model. The lack of scale separation in rocks represents a limitation for their application. The solutions provided are not accurate since they fail to preserve details of the rock's physical properties.

Limitations of the upscaling methods are overcome with the multiscale methods [23] that depend on the computation of basis functions. They have also denominated prolongation operators and are defined as functions that permit the transfer of the solution in a coarse grid version of the model to the fine-scale grid.

There is extensive literature developed around multiscale methods. Multiscale finite element (MSFE) ([22] [11]) use a set of reduced boundary conditions formulated to separate each coarse volume in the primal grid to solve the basis functions. The basis-functions avoid considering the normal component of the flux on the surface of the coarse volumes that leads to obtaining velocity fields that are not conservative. Multiscale mixed finite element (MSMFE) ([4] [8] [3] [1] [2]) method generates basis functions that calculate at the same time the pressure and velocity fields. The multiscale finite volume (MSFV) ([23] [24] [35] [31] [36] [19] [56] [25] [37] [15] [16] [38] [17] [57] [54] [42]) method calculates the basis-functions in a dual grid. The calculated basis functions are non-conservative on each dual grid block's surface, but they are conservative on each of them's fine-scale system domain. A new set of basis functions is calculated on each primal coarse block's surface to reconstruct a conservative velocity field.

To be practical in the industry, the multiscale methods should be developed in realistic reservoir structures and handle the grid geometry complexity and flow physics. Cartesian grids do not model geological characteristics such as faults and stratigraphic features. Unstructured grids can model these features, but the primal and dual coarse grid's generation in these grids involves several challenges ([41] [42] [48]). Recent work has been done to solve the effect of high heterogeneity and anisotropy ratios in the MSFV solutions [55]. Corner point grids, a stratigraphic grid, can also replicate geological features and challenges that arise in defining the primal and dual coarse grid in these grids in reservoir models with degenerated and irregular grid cells.

Based on the restrictions to define a method to properly generate primal and dual coarse grids in different types of grids, the Multiscale Restriction-Smoothed Basis (MsRSB) [42] method avoids the definition of the dual coarse grid. The basis functions are determined iteratively and defined a support region for each of them. The original MsRSB formulation used the two-point flux approximation (TPFA) as a discretization method. Recently, work has been done to overcome the limitation of the TPFA on non-orthogonal grids. A Multipoint Flux Approximation with a Diamond stencil has been applied to

extend the method to general unstructured grids [9]. MsRSB has been extended to applications to porous media flow and geomechanics [7].

In this appendix, an introduction to MSFV in corner point grid models is explained. It starts with basic concepts about MSFV; results are shown for the primal coarse grid partition in several test cases.

A.1. Fine-scale discretized system: single phase flow

Single-phase incompressible flow in the absence of gravity can be described using Darcy's law as

$$-\nabla \cdot (\lambda \cdot \nabla p) = q \tag{A.1}$$

whereλ is the mobility, p the fluid pressure, and q denotes the source terms. Equation A.1 is discretized for every matrix cell control volume using a two-point flux approximation scheme,

$$u_{ij} = T_{ij}\ (p_i - p_j) \tag{A.2}$$

where T_{ij} is the transmissibility related with the interface shared between cells i and j. The resultant linear system corresponding to equation A.2 reads.

$$A\ p = q \tag{A.3}$$

A.2. MSFV on corner point grids

MSFV solves a coarse system constructed using local basis functions to estimates the fine scale solution. Basis functions are solved on a dual-coarse grid, but the method also depend on a primal coarse grid to build a conservative coarse-scale system. Hence, extending the MSFV to structured grids (corner point grids) involves the suitable construction of primal and dual coarse grids. It has been shown how the MSFV method can be extended to corner point grids with faults and distorted cells [41].

A.2.1. MSFV formulation

The multiscale finite volume method provides an estimated solution to equation A.3. If the coarse pressure p_c is calculated in the coarse grid, the fine scale pressure p can be approximated by the multiscale solution p' with the use of the prolongation operator $\boldsymbol{P}$ (matrix of basis functions)

$$p \approx p' = \boldsymbol{P}\ p_c \tag{A.4}$$

The coarse-scale pressure p_c is obtained by solving the coarse-scale system $A_c\ p_c = q_c$, which is built algebraically as

$$\underbrace{(\boldsymbol{R}A\boldsymbol{P})}_{A_c}\ p_c = \underbrace{\boldsymbol{R}\ q}_{q_c}. \tag{A.5}$$

Here, $\boldsymbol{R}$ is the restriction and $\boldsymbol{P}$ the prolongation operators. The restriction operator $\boldsymbol{R}$ brings the fine-scale solution to the coarse-scale, resulting in a decrease of unknowns. For a finite-volume-based multiscale formulation (MSFV), the restriction operator characterizes the integration operator over the coarse-grid cells, i.e., for its entry $R(i,j)$, one can define

$$R_{i,j} = \begin{cases} 1 & \text{fine cell j} \in \text{to coarse cell i} \\ 0 & \text{otherwise} \end{cases} \tag{A.6}$$

Therefore, $\boldsymbol{R}$ is a matrix of size $N_c \times N_f$ where N_c and N_f are the number of coarse and fine cells, respectively. The prolongation operator $\boldsymbol{P}$ contains the basis functions, Φ , which groups all of them into its columns, i.e.,

$$\boldsymbol{P} = \begin{bmatrix} \cdot & \cdot & \cdot \\ \cdot & \cdot & \cdot \\ \cdot & \cdot & \cdot \\ \Phi_1^m & \dots \Phi_i^m \dots & \Phi_{N_{mc}}^m \\ \cdot & \cdot & \cdot \\ \cdot & \cdot & \cdot \\ \cdot & \cdot & \cdot \end{bmatrix}_{N_f \times N_c} \tag{A.7}$$

Basis functions are local interpolators that capture the complex fine-scale solution in a coarse node's surrounding area. For each coarse node exists one basis function, and the dual-coarse grid defines their local support region.

A.2.2. Primal Grid

The construction of prolongation and restriction operators requires the generation of primal and dual coarse grids. METIS [14] is used to obtain the primal grids. This partition represents the coarse grid, and the fine-scale connectivity (transmissibility) was the input to get the primal division. METIS allows additional inputs to improve the fine-scale grid's partition by using weights (e.g., permeability) or partitioning criteria.

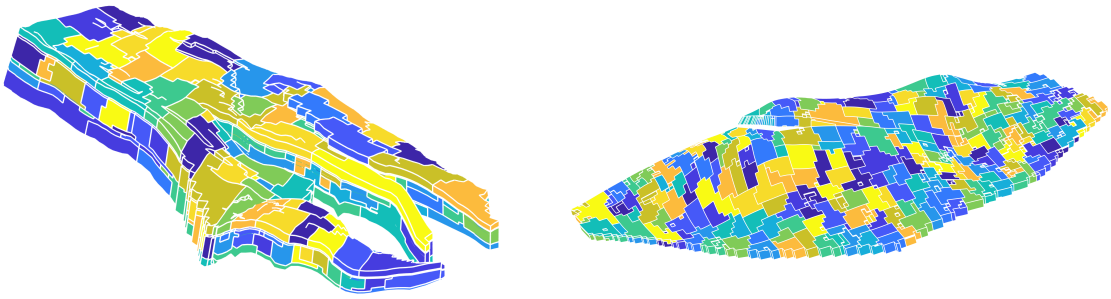

(a) Norne Field: 250 primal coarse grid cells (44915 fine cells).

(b) Brugge Model: 250 primal coarse grid cells (43474 fine cells).

Figure A.1: Primal Coarse Grid Partition: Norne Field | Brugge Model.

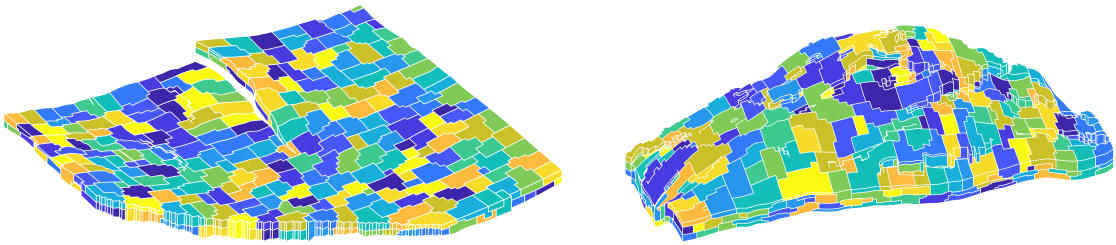

(a) Johansen Formation: 500 primal coarse grid cells (88775 fine cells)

(b) SAIGUP Model: 450 primal coarse grid cells (78720 fine cells)

Figure A.2: Primal Coarse Grid Partition: Johansen formation | SAIGUP model.

A.2.3. Dual Grid

First, a fine cell should be selected as the coarse node (dual-node) inside each coarse cell to construct the dual-grid. The classical MSFV approach designates the fine-scale volume closest to the centroid of the primal coarse as the coarse node. Numerical experiments have shown that rather than establishing the block centroid as the block center, it should choose the block centroid as the fine cell whose centroid is closest to the geometric median of the fine-scale faces that bound the block. The two options coincide in regular coarse grids, but the geometric median gives basis functions of better quality for coarse partitions with a significant discrepancy in block sizes and shapes.

In [42], a three-step algorithm is proposed to select the coarse node. Figure A.3 shows the process in an unstructured coarse mesh. The first step is to find the interfaces between the purple coarse volume and its neighbors. Second, the middle of these interfaces is calculated by finding the point that splits in two of each interface's length. Finally, the middle points are used to determine the Geometric Median. The geometric median finds a point that reduces the sum of the distances of the sampled

points. The center point of a coarse volume is the point that has the lowest sum of distances to the middle edges interfaces. The center of a primal coarse volume is the fine-scale cell whose center coordinates are closest to its geometric median.

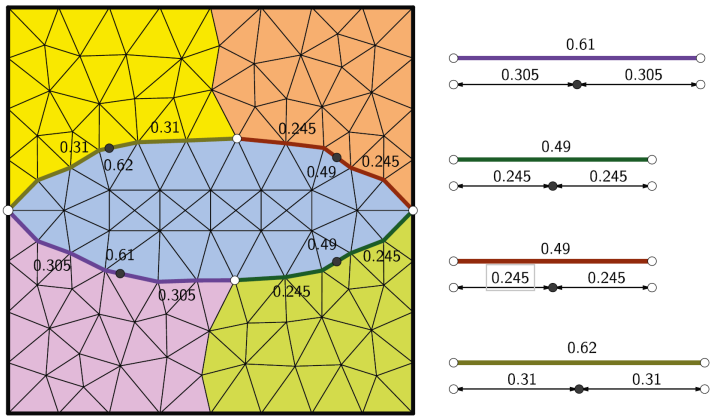

Figure A.3: Detection of the center of the interfaces (Source: de Souza (2020)).

Bibliography

[1] Efendiev Y. Aarnes J.E. An adaptive multiscale method for simulation of fluid flow in heterogeneous porous media. *Multiscale Modeling Simulation*, 5:918–939, 2006.

[2] Jiang L. Aarnes J.E., Efendiev Y. Mixed multiscale finite element methods using limited global information. *Multiscale Modeling Simulation*, 7:655–676, 2008. doi: 10.1137/070688481.

[3] Lie K.A. Aarnes J.E., Kippe V. Mixed multiscale finite elements and streamline methods for reservoir simulation of large geomodels. *Advances in Water Resources*, 28(3):257–271, 2005. doi: 10.1016/j.advwatres.2004.10.007.

[4] T. Arbogast. Implementation of a locally conservative numerical subgrid upscaling scheme for two-phase darcy flow. *Computational Geosciences*, 6:453–481, 2002. doi: 10.1023/A:1021295215383.

[5] K. Aziz and A. Settari. *Petroleum Reservoir Simulation*. Blitzprint Ltd., Cagary, Alberta, 2002.

[6] B. Berkowitz. Characterizing flow and transport in fractured geological media: A review. *Physica B: Condensed Matter*, 25:861–884, 2002. doi: 10.1016/S0309-1708(02)00042-8.

[7] Moyner O. Castelletto N. Bosma S., Klevtsov S. Enhanced multiscale restriction-smoothed basis (msrsb) preconditioning with applications to porous media flow and geomechanics. *Journal of Computational Physics*, 109934, 2020. doi: 10.1016/j.jcp.2020.109934.

[8] Hou T.Y. Chen, Z.M. A mixed multiscale finite element method for elliptic problems with oscillating coefficients. *Mathematics of Computation*, 72:541–576, 2003.

[9] de Souza A.C.R.; Barbosa L.M.C.; Contreras F.R.L.; Lyra P.R.M. and Carvalho D.K.E. A multiscale control volume framework using the multiscale restriction smooth basis and a non-orthodox multipoint flux approximation for the simulation of two-phase flows on truly unstructured grids. *Journal of Petroleum Science and Engineering*, 188(106851), 2020. doi: 10.1016/j.petrol.2019.106851.

[10] Y. Ding and P. Lemonnier. Use of corner point geometry in reservoir simulation. *Presented at the International Meeting on Petroleum Engineering, Beijing, China, 14–17 November*, SPE-29933-MS, 1995. doi: 10.2118/29933-MS.

[11] Hou T.Y Efendiev, Y. Multiscale finite element methods. theory and applications. *Springer-Verlag New York*, 2009. doi: 10.1007/978-0-387-09496-0.

[12] H.; Hellevang B.; Riis F.; Johansen W.; Eigestad, G.; Dahle and E. Øian. Geological modeling and simulation of co2 injection in the johansen formation. *Computational Geosciences*, 13(1):435–450, 2009. doi: 10.1007/s10596-009-9153-y.

[13] C. L. Farmer. Upscaling: a review. *International Journal for Numerical Methods in Fluids.*, 40:63–78, 2002. doi: 10.1002/fld.267.

[14] Karypis G. Metis– serial graph partitioning and fill-reducing matrix ordering, tech. rep. version 5.1.0. *Karypis Lab, University of Minnesota*, 2013.

[15] Bonfigli G. Hesse M.A. Jenny P. Hajibeygi, H. Iterative multiscale finite-volume method. *Journal of Computational Physics*, 227:8604–8621, 2008. doi: 10.1016/j.jcp.2008.06.013.

[16] Jenny P. Hajibeygi, H. Multiscale finite-volume method for parabolic problems arising from compressible multiphase flow in porous media. *Journal of Computational Physics*, 228:5129–5147, 2009. doi: 10.1016/j.jcp.2009.04.017.

[17] Jenny P. Hajibeygi, H. Adaptive iterative multiscale finite volume method. *Journal of Computational Physics*, 230–:628–643, 2011. doi: 10.1016/j.jcp.2010.10.009.

[18] Karvounis D. Jenny P. Hajibeygi, H. A hierarchical fracture model for the iterative multiscale finite volume method. *Journal of Computational Physics*, 230(24):8729–8743, 2011. doi: 10.1016/j.jcp.2011.08.021.

[19] Mallison B.T. Tchelepi H.A. Hesse, M.A. Compact multiscale finite volume method for heterogeneous anisotropic elliptic equations. *Multiscale Modeling Simulation*, 7:934–962, 2008.

[20] Vuik C. HosseiniMehr, M. and H. Hajibeygi. Adaptive dynamic multilevel simulation of fractured geothermal reservoirs. *Journal of Computational Physics: X*, 7, 2020a. doi: 10.1016/j.jcpx.2020.100061.

[21] Vuik C. HosseiniMehr, M. and H. Hajibeygi. Adaptive dynamic multilevel simulation of fractured geothermal reservoirs. *Journal of Computational Physics: X*, 7, 2020b. doi: 10.1016/j.jcpx.2020.100061.

[22] Wu X.H. Hou, T.Y. A multiscale finite elementmethod for elliptic problems in composite materials and porous media. *Journal of Computational Physics*, 134:169–189, 1997. doi: 10.1006/jcph.1997.5682.

[23] Lee S.H. Tchelepi H.A. Jenny, P. Multiscale finite-volume method for elliptic problems in subsurface flow simulation. *Journal of Computational Physics*, 187(1):47–67, 2003. doi: 10.1016/S0021-9991(03)00075-5.

[24] Lee S.H. Tchelepi H.A. Jenny, P. Adaptive fully implicit multiscale finite-volume method for multiphase flow and transport in heterogeneous porous media. *Journal of Computational Physics*, 217(2):627–641, 2006. doi: 10.1016/j.jcp.2006.01.028.

[25] Lunati I. Jenny, P. Modeling complex wells with the multi-scale finite-volume method. *Journal of Computational Physics*, 228(3):687–702, 2009. doi: 10.1016/j.jcp.2008.09.026.

[26] Younis R.M. Jiang, J. Hybrid coupled discrete-fracture/matrix and multicontinuum models for unconventional-reservoir simulation. *SPE Journal*, 21(3), 2016. doi: 10.2118/178430-PA.

[27] Younis R.M. Jiang, J. An improved projection-based embedded discrete fracture model (pedfm) for multiphase flow in fractured reservoirs. *Advances in Water Resources*, 109:267–289, 2017. doi: 10.1016/j.advwatres.2017.09.017.

[28] K.Aziz Karimi-Fard, L. Durlofsky. An efficient discrete-fracture model applicable for general-purpose reservoir simulators. *SPE Journal*, 2004. doi: 10.2118/88812-PA.

[29] Lough M.F. Jensen C.L. Lee, S.H. Efficient finite-difference model for flow in a reservoir with multiple length-scale fractures. *SPE Journal*, 5(3), 2000. doi: 10.2118/65095-PA.

[30] Lough M.F. Jensen C.L. Lee, S.H. Hierarchical modeling of flow in naturally fractured formations with multiple length scales. *Water Resource Research*, 37(3):443–455, 2001. doi: 10.1029/2000WR900340.

[31] Wolfsteiner C. Tchelepi H.A. Lee, S.H. Multiscale finite-volume formulation for multiphase flow in porous media: black oil formulation of compressible, three-phase flow with gravity. *Computational Geosciences*, 12(3):351–366, 2008. doi: 10.1007/s10596-007-9069-3.

[32] Lee S.H. Li, L. Efficient field-scale simulation of black oil in naturally fractured reservoir through discrete fracture networks and homogenized media. *SPE Reservoir Evaluation Engineering*, 11:750–758, 2008. doi: 10.2118/103901-PA.

[33] K.A. Lie. An introduction to reservoir simulation using matlab/gnu octave: User guide for the matlab reservoir simulation toolbox (mrst). *Cambridge University Press*, 2019. doi: 10.1017/9781108591416.

[34] Mykkeltvedt T. S. Møyner O. Lie, K.A. A fully implicit weno scheme on stratigraphic and unstructured polyhedral grids. *Computational Geosciences*, 24:405–423, 2020. doi: 10.1007/s10596-019-9829-x.

[35] Jenny P. Lunati, I. Multiscale finite-volume method for compressible multiphase flow in porous media. *Journal of Computational Physics*, 216(2):616–636, 2006. doi: 10.1016/j.jcp.2006.01.001.

[36] Jenny P. Lunati, I. Multiscale finite-volume method for density driven flow in porous media. *Computational Geosciences*, 12(3):337–350, 2008. doi: 10.1007/s10596-007-9071-9.

[37] Lee S.H. Lunati, I. An operator formulation of the multiscale finite-volume method with correction function. *Multiscale Modeling Simulation*, 8(1):96–109, 2009. doi: 10.1137/080742117.

[38] Tyagi M. Lee S.H. Lunati, I. An iterative multiscale finite volume algorithm converging to the exact solution. *Journal of Computational Physics*, 230–:1849–1864, 2011. doi: 10.1016/j.jcp.2010.11.036.

[39] et al. Manzocchi, T. Sensitivity of the impact of geological uncertainty on production from faulted and unfaulted shallow-marine oil reservoirs: Objectives and methods. *Petroleum Geoscience*, 14(1):3–15, 2008. doi: 10.1144/1354-079307-790.

[40] Narr W. Hui M. Mallison B.T. Lee S.H. Moinfar, A. Comparison of discrete-fracture and dual-permeability models for multiphase flow in naturally fractured reservoirs. *SPE Reservoir Simulation Symposium, 21-23 February, The Woodlands, Texas, USA*, 2011. doi: 10.2118/142295-MS.

[41] Lie K.A. Moyner, O. The multiscale finite volume method on stratigraphic grids. *SPE Journal*, 19:816–831, 2014. doi: 10.2118/163649-PA.

[42] Lie K.A. Moyner, O. A multiscale restriction-smoothed basis method for high contrast porous media represented on unstructured grids. *Journal of Computational Physics*, 304:46–71, 2016. doi: 10.1016/j.jcp.2015.10.010.

[43] Open Porous Media (OPM). http://opm-project.org.

[44] Arts R. Brouwer G. et al. Peters, L. Results of the brugge benchmark study for flooding optimization and history matching. *SPE Reservoir Evaluation Engineering*, 294–295:391–405, 2010. doi: 10.2118/119094-PA.

[45] D.K. Ponting. Corner point geometry in reservoir simulation. *Presented at the 1st European Conference on the Mathematics of Oil Recovery, Cambridge, UK, 14–16 July*, 1989.

[46] S. Lamine B. A. H. Huisman M. Pal R. Ahmed, M. G. Edwards. Control-volume distributed multi-point flux approximation coupled with a lower-dimensional fracture model. *Journal of Computational Physics*, 284:462–489, 2015. doi: 10.1016/j.jcp.2014.12.047.

[47] Jiang J. Younis R.M. Ren, G. A model for coupled geomechanics and multiphase flow in fractured porous media using embedded meshes. *Advances in Water Resources*, 122:113–130, 2018. doi: 10.1016/j.advwatres.2018.09.017.

[48] Bosma S., Hajibeygi H., Tene M., and Tchelepi H.A. Multiscale finite volume method for discrete fracture modeling on unstructured grids (ms-dfm). *Journal of Computational Physics*, 351:145–164, 2017. doi: 10.1016/j.jcp.2017.09.032.

[49] Schlumberger. Eclipse reference manual. 2014.

[50] Bosma S. B. Hajibeygi H. Al Kobaisi M. S. et al Tene, M. Projection-based embedded discrete fracture model (pedfm). *Advances in Water Resources*, 105:205–216, 2017. doi: 10.1016/j.advwatres.2017.05.009.

[51] P. Bastian R. Helmig V. Reichenberger, H. Jakobs. A mixed-dimensional finite volume method for two-phase flow in fractured porous media. *Advances in Water Resources*, 29(7):1020–1036, 2006. doi: 10.1016/j.advwatres.2005.09.001.

[52] Hetland M. Verlo, S. B. Development of a field case with real production and 4d data from the norne field as a benchmark case for future reservoir simulation model testing. msc thesis. *Norwegian University of Science and Technology, Trondheim, Norway*, 2008.

[53] W. A. Wadsley. Pmodelling reservoir geometry with non-rectangular coordinate grids. *Presented at the SPE Annual Technical Conference and Exhibition, Dallas, Texas, 21–24 September*, SPE-9369-MS, 1980. doi: 10.2118/9369-MS.

[54] Hajibeygi H. Tchelepi H.A. Wang, Y. Algebraic multiscale solver for flow in heterogeneous porous media. *Journal of Computational Physics*, 259:284–303, 2014. doi: 10.1016/j.jcp.2013.11.024.

[55] Mehrdoost Z. Unstructured grid adaptation for multiscale finite volume method. *Computational Geosciences*, 23:1293–1316, 2019. doi: 10.1007/s10596-019-09878-9.

[56] Tchelepi H.A. Zhou, H. Operator-based multiscale method for compressible flow. *SPE Journal*, 23–:267–273, 2008. doi: 10.2118/106254-PA.

[57] Tchelepi H.A. Zhou, H. Two-stage algebraic multiscale linear solver for highly heterogeneous reservoir models. *SPE Journal*, 17:523–539, 2012. doi: 10.2118/141473-PA.